Evolution of Einstein-scalar-Gauss-Bonnet gravity using a modified harmonic formulation

William E. East[1,*] and Justin L. Ripley [2,†]

[1]*Perimeter Institute for Theoretical Physics, Waterloo, Ontario N2L 2Y5, Canada*
[2]*DAMTP, Centre for Mathematical Sciences, University of Cambridge,
Wilberforce Road, Cambridge CB3 0WA, United Kingdom*

We present numerical solutions of several spacetimes of physical interest, including binary black hole mergers, in shift-symmetric Einstein-scalar-Gauss-Bonnet (ESGB) gravity, and describe our methods for solving the full equations of motion, without approximation, for general spacetimes. While we concentrate on the specific example of shift-symmetric ESGB, our methods, which make use of a recently proposed modification to the generalized harmonic formulation, should be generally applicable to all Horndeski theories of gravity (including general relativity). We demonstrate that these methods can stably follow the formation of scalar clouds about initially vacuum nonspinning and spinning black holes for values of the Gauss-Bonnet coupling approaching the maximum value above which the hyperbolicity of the theory breaks down in spherical symmetry. We study the collision of black holes with scalar hair, finding that the theory remains hyperbolic in the spacetime region exterior to the black hole horizons in a similar regime, which includes cases where the deviations from general relativity in the gravitational radiation is appreciable. Finally, we demonstrate that these methods can be used to follow the inspiral and merger of binary black holes in full ESGB gravity. This allows for making predictions for Horndeski theories of gravity in the strong-field and nonperturbative regime, which can confronted with gravitational wave observations, and compared to approximate treatments of modifications to general relativity.

I. INTRODUCTION

With the advent of gravitational wave astronomy, we are now in an unprecedented position to test whether general relativity (GR) provides an accurate description of gravity in the strong-field, highly dynamical regime. Observations of black hole and other compact object mergers have already been used to constrain a number of deformations of GR, including extra gravitational wave polarizations, a graviton mass, and Lorentz violations [1]. Despite these observational successes, for many alternative theories, it is still unclear whether they are even on an equal theoretical footing to GR, in the sense of being able to provide a full prediction of what happens when two black holes merge.

Determining which theories that modify the principle part of the Einstein equations are predictive in the strong-field regime (in the mathematical sense that they have a well-posed initial value problem) has been a pressing question in efforts to test such theories with observations. Some theories, for example dynamical Chern-Simons [2–4], or theories that introduce Riemann-to-the-fourth-power type terms in the action [5,6], no longer have second

order equations of motion (EOMs), which is a requirement for a theory to be Ostrogradsky stable [7]. Thus one has little choice but to treat such theories as valid on some limited range of scales and to perturbatively solve for the dynamics of those theories. In contrast, here we will concentrate on Einstein-scalar-Gauss Bonnet (ESGB), which is a representative example of a Horndeski gravity theory. Horndeski gravity theories are the class of classical scalar-tensor theories that have second order EOMs [8] and thus can be thought of as the widest possible class of scalar-tensor gravity theories that could act as classical, theoretically viable alternatives to GR. Given this, Horndeski theories could be employed in *model dependent* tests of GR using gravitational wave observations of black holes and neutron star binaries (for a recent review see, e.g. [9]).

As an alternative to thinking of modified gravity theories as complete classical field theories, the same as GR, one can view them as *effective field theories* (EFTs) that parametrize small deviations as a derivative expansion from GR (for reviews see, e.g. [10,11]). The dynamics of EFTs are naturally solved in terms of an *order reduction* approach, where small corrections to Einstein evolution are solved for order by order in terms of the effective coupling parameters. However, even taking this viewpoint, there are reasons to study exact solutions to Horndeski gravity

*weast@perimeterinstitute.ca
†lloydripley@gmail.com

theories. While not all potential effective deviations from GR are Horndeski theories (such as dynamical Chern-Simons gravity), a subclass of Horndeski gravity theories called "four derivative scalar-tensor theory" (4∂ST) gravity encompasses the leading order scalar-tensor interactions that are parity invariant [12]. One challenge with computing dynamical solutions to EFTs through an order reduction approach is that the solution can be contaminated by secular effects, which are purely artifacts of the order reduction approximation, but which can grow in time. There have been some proposals to address these problems [13,14], including by changing the behavior of the theory at short wavelengths in an *ad hoc* manner in order to cure problems with well-posedness [15]. However, without full solutions to compare to, it is difficult to quantify the errors introduced by these methods. Stable numerical solutions to the exact EOMs would not be subject to those kinds of secular effects. For small enough modified gravity couplings, exact solutions could be used to find essentially perturbative corrections to the Einstein equations, while avoiding spurious contamination of the solution from secular errors.

One technical challenge that has prevented finding fully nonlinear solutions to many Horndeski gravity theories for spacetimes that lack any symmetries (as is the case for binary black hole merger spacetimes) has been that there was no known well-posed initial formulation for Horndeski gravity. Recently though, Kovacs and Reall proved that the equations of motion for Horndeski gravity theories possess a well posed initial value problem in a *modified harmonic formulation* [16,17],[1] as long as the coupling parameter that determines the beyond-GR corrections is much smaller than all other length scales in the problem. Their result has opened up the possibility for full numerical simulations of Horndeski gravity theories for spacetimes of physical interest, such as binary black hole spacetimes, and for cosmologies that are not perfectly homogeneous. However, determining for what range of couplings this formulation is hyperbolic for strong-field, dynamical spacetimes is something that most likely needs to be done on case-by-case basis numerically, for different Horndeski theories and choices of initial data.

Here, we numerically solve for the dynamics of black holes in *shift-symmetric* ESGB gravity. Shift-symmetric ESGB gravity has attracted recent interest as the Schwarzschild and Kerr black hole solutions of GR are not stationary solutions to this theory [20]: vacuum black holes will evolve to black hole solutions with stable scalar field clouds (i.e. scalar hair) around them. Disregarding Horndeski models that model dark energy (many of which

have been highly constrained, see e.g. [21–23]), ESGB gravity have attracted recent attention as the couplings for the theory are relatively weakly constrained, yet the theory admits scalar hairy black hole solutions (see e.g. [24,25]), the collision of which should produce gravitational wave signals that differ noticeably from those of GR black holes. ESGB gravity thus promises to act as a useful foil to perform model dependent tests of GR in the strong field, dynamical regime (for further discussion see, e.g., [26]).

Shift symmetric ESGB gravity can be motivated as the leading order scalar tensor theory of gravity whose equations of motion are invariant under shifts in the scalar field: $\phi \rightarrow \phi + \text{const}$ [12,25].[2] While there is an EFT argument to motivate this theory, we solve for the full equations of motion without any perturbative assumptions, potentially outside the regime of validity of the assumptions of EFT. While in this article we only consider numerical solutions to shift-symmetric ESGB gravity, for general interest we also present the equations of motion for the leading order scalar tensor theory of gravity whose equations of motion are invariant under parity inversion: $x^a \rightarrow -x^a$ (4∂ST gravity), in a form suitable for use in modified harmonic evolution.

Earlier studies of shift-symmetric ESGB gravity have been limited to either spacetimes with a high degree of symmetry (e.g. [20,27,28]), stationary solutions [29,30], or to perturbative/order reduction solutions to the theory (e.g. [14,31–34]). In Refs. [27,28], it was found that in spherical symmetry, for sufficiently large values of the Gauss-Bonnet coupling, black hole spacetimes could develop elliptic regions, where the hyperbolicity of the equations broke down, outside the black hole horizon. This sets an upper bound for the range of parameters where the theory will remain hyperbolic once spherical symmetry is broken.

In this paper, we describe our methods for numerically solving the full equations of ESGB gravity and use them to study the dynamics of black hole scalar hair formation and black hole mergers. One of our main results is that we find that we are able to solve for spacetimes where the deviations from GR are significant in terms of the changes to the black holes due to dynamical scalar hair formation, and the imprint on the gravitational waves. The remainder of the paper is as follows. In Sec. II A, we present the EOMs for the general class of 4∂ST gravity (which includes ESGB) in the form we use for numerical evolutions. In Sec. III, we describe our numerical methods for evolving these equations. In Sec. IV, we presents our results, beginning with a robustness test to illustrate the improved hyperbolicity, and then moving on to several physically interesting problems including the dynamical formation of scalar hair about spinning black holes in

---

[1]We note that a different gauge condition was proven to provide a well-posed initial problem for "cubic" Horndeski theories (which do not include ESGB) by Kovacs [18], and that gauge condition was numerically implemented in Ref. [19] to study spherical collapse in that class of theories.

[2]Although in this paper, for simplicity we do not consider *all* terms allowed by shift symmetry; in particular we do not consider the term αX^2; see Eq. (5).

axisymmetry and a fully 3D setting, and head-on and quasicircular binary black hole mergers. We discuss these results and conclude in Sec. V.

In this work we use geometric units: $G = c = 1$, a metric sign convention of $-+++$, lower case latin letters to index spacetime indices, and lower case greek letters to index spatial indices.

II. EQUATIONS OF MOTION

A. Modified generalized harmonic formulation

We begin by briefly reviewing the modified generalized harmonic (MGH) formulation [16,17]. In a Lorentzian spacetime (M, g), we introduce two auxiliary Lorentzian metrics $\tilde{g}^{mn}$ and $\hat{g}^{mn}$. We will always raise and lower indices with the spacetime metric g_{ab}, so e.g. $\hat{g}^{ab} \equiv g^{ac}g^{bd}\hat{g}_{cd}$. We also define $\tilde{g} \equiv \tilde{g}^{ab}g_{ab}$ and $\hat{g} \equiv \hat{g}^{ab}g_{ab}$. The MGH formulation imposes the following conditions on the coordinates x^c:

$$C^c \equiv H^c - \tilde{g}^{ab}\nabla_a\nabla_b x^c = H^c + \tilde{g}^{ab}\Gamma^c_{ab} = 0. \quad (1)$$

As in the generalized harmonic formulation, H^c are the source functions that, along with $\tilde{g}^{ab}$, determine the gauge degrees of freedom, and C^c (which will generally not be exactly zero in a given numerical solution) is called the *constraint violation*. We next define the MGH EOMs as

$$E^{ab} - \hat{P}_d{}^{cab}\nabla_c C^d - \frac{1}{2}\kappa(n^a C^b + n^b C^a + \rho n^c C_c g^{ab}) = 0, \quad (2)$$

where E^{ab} are the EOMs derived from varying the metric, n^a is a timelike vector (we assume n^a is timelike with respect to g^{ab}, $\tilde{g}^{ab}$, and $\hat{g}^{ab}$), and

$$\hat{P}_d{}^{cab} \equiv \frac{1}{2}(\delta^a_d\hat{g}^{bc} + \delta^b_d\hat{g}^{ac} - \delta^c_d\hat{g}^{ab}). \quad (3)$$

We include constraint damping with the constants κ and ρ [35].[3] Note as well that Eq. (2) is slightly different from Ref. [17]: here we use $\nabla_c C^d$ instead of $\partial_c C^d$. We choose the form used here for consistency with the standard generalized harmonic formulation (see Appendix C), though either way the principal part, and hence the hyperbolicity results, will be the same. From Eq. (1), we see that in the MGH formulation the coordinates x^a obey a hyperbolic equation with characteristics determined by $\tilde{g}^{ab}$. Taking the divergence of Eq. (2), and assuming $\nabla_a E^{ab} = 0$ (which holds for all the theories we consider, including the Einstein equations), we obtain a hyperbolic equation for the constraint violating modes C^a,

$$-\frac{1}{2}\hat{g}^{ac}\nabla_a\nabla_c C^b - \hat{g}^{cb}R_{dc}C^d - (\nabla_a\hat{P}_d{}^{cab})(\nabla_c C^d)$$
$$-\frac{1}{2}\kappa\nabla_a(n^a C^b + n^b C^a + \rho n^c C_c g^{ab}) = 0. \quad (4)$$

From Eq. (4), we see that the constraint violating modes obey a hyperbolic equation with characteristics determined by $\hat{g}^{ab}$. With the special choice of $\tilde{g}^{ab} = \hat{g}^{ab} = g^{ab}$, the MGH formulation reduces to the generalized harmonic formulation (for an explicit calculation of this in the context of the Einstein equations, see Appendix C). Finally, we note that picking a gauge in the MGH formulation amounts to choosing the functional form of the auxiliary metrics $\tilde{g}^{ab}$ and $\hat{g}^{ab}$, and choosing the functional form of the source function H^c.

B. Equations of four derivative scalar tensor (4∂ST) gravity for a modified harmonic formulation

While we only consider numerical solutions to shift-symmetric ESGB gravity in this article, we derive the EOMs in the MGH formulation for the following scalar-tensor theory (Kovacs and Reall call 4∂ST gravity [16,17]), for which ESGB gravity is a specific example. We do this for the sake of generality and given the applications of 4∂ST gravity in, e.g., EFTs of the early Universe (e.g. [12]). The action is

$$S = \frac{1}{8\pi}\int d^4x\sqrt{-g}\left(\frac{1}{2}R + X - V(\phi) + \alpha(\phi)X^2 + \beta(\phi)\mathcal{G}\right), \quad (5)$$

where

$$X \equiv -\frac{1}{2}(\nabla\phi)^2, \quad (6a)$$

$$\mathcal{G} \equiv \frac{1}{4}\delta^{abcd}_{efgh}R^{ef}{}_{ab}R^{gh}{}_{cd}, \quad (6b)$$

$$\delta^{abcd}_{efgh} \equiv 4!\delta^a_{[e}\delta^b_f\delta^c_g\delta^d_{h]}, \quad (6c)$$

and V, α, and β are functions of ϕ. If one interprets Eq. (5) as an EFT, it contains (up to total derivatives, field redefinitions, and conformal rescalings) all scalar-tensor terms involving up to four derivatives. Thus, from an EFT perspective, the theory represents the leading order (in derivatives) scalar-tensor theory that is preserved under parity transformations [12,16,17].[4]

---

[3]Note that we need $\kappa < 0$ to damp out the constraints. Also, some of our sign conventions differ from [17].

[4]For more context regarding the theory we consider: Ref. [12] considered the Weyl tensor coupling $f(\phi)C_{abcd}C^{abcd}$, which when varied in the action leads to fourth order equations of motion, which likely do not have a well-posed initial value formulation when taken as classical PDE. References [16,17] pointed out that if (through field redefinitions) one replaces $C_{abcd}C^{abcd}$ with the Gauss-Bonnet scalar $\mathcal{G}$, then the EOMs are second order in time and space, and furthermore have a well-posed initial value problem in the MGH formulation.

We obtain shift-symmetric ESGB gravity by choosing $V(\phi) = \alpha(\phi) = 0$ and $\beta(\phi) = \lambda\phi$. Here λ is a constant coupling parameter, that in geometric units has dimensions of length squared. As the Gauss-Bonnet scalar $\mathcal{G}$ is a total derivative in four dimensions, we see that the action of shift-symmetric ESGB gravity is preserved up to total derivatives under constant shifts in the scalar field: $\phi \to \phi + $ constant.

Varying Eq. (5) with respect to the scalar field and metric gives us the EOMs,

$$E^{(\phi)} \equiv \Box\phi - V'(\phi) + 2\alpha(\phi)X\Box\phi - 2\alpha(\phi)\nabla^a\phi\nabla^b\phi\nabla_a\nabla_b\phi$$
$$- 3\alpha'(\phi)X^2 + \beta'(\phi)\mathcal{G} = 0, \qquad (7)$$

$$E^{(g)}_{ab} \equiv R_{ab} - \frac{1}{2}g_{ab}R - \nabla_a\phi\nabla_b\phi + (-X + V(\phi))g_{ab}$$
$$- 2\alpha(\phi)X\nabla_a\phi\nabla_b\phi - \alpha(\phi)X^2 g_{ab}$$
$$+ 2\delta^{efcd}_{ijg(a}g_{b)d}R^{ij}_{\ \ ef}\nabla^g\nabla_c\beta(\phi) = 0. \qquad (8)$$

We take the trace-reverse of Eq. (8) to obtain

$$E^{(g,TR)}_{ab} \equiv E^{(g)}_{ab} - \frac{1}{2}g_{ab}E^{(g)}$$
$$= R_{ab} - \nabla_a\phi\nabla_b\phi - V(\phi)g_{ab}$$
$$- 2\alpha(\phi)X\nabla_a\phi\nabla_b\phi - \alpha(\phi)X^2 g_{ab}$$
$$+ 2\delta^{efcd}_{ijg(a}g_{b)d}R^{ij}_{\ \ ef}\nabla^g\nabla_c\beta(\phi)$$
$$- \delta^{efc}_{ijg}R^{ij}_{\ \ ef}\nabla^g\nabla_c\beta(\phi)g_{ab}. \qquad (9)$$

The last step we take before expanding out the EOMs is to add in the MGH constraint propagation term and a constraint damping term [17,35],

$$E^{(g,C)}_{ab} \equiv E^{(g,TR)}_{ab} - \left(\hat{P}_c^{\ d}{}_{ab} - \frac{1}{2}g_{ab}\hat{P}_c^{\ d}\right)\nabla_d C^c$$
$$- \frac{1}{2}\kappa(n_a C_b + n_b C_a - (1+\rho)n_c C^c g_{ab}), \qquad (10)$$

where we have defined $\hat{P}_d^{\ c} \equiv g_{ab}\hat{P}_d^{\ cab}$.

Finally, we rewrite the 4∂ST EOMs, Eqs. (9) and (10), in the following form:

$$\begin{pmatrix} A_{ab}{}^{cd} & B_{ab} \\ C^{cd} & D \end{pmatrix}\partial_0^2\begin{pmatrix} g_{cd} \\ \phi \end{pmatrix} + \begin{pmatrix} F^{(g)}_{ab} \\ F^{(\phi)} \end{pmatrix} = 0. \qquad (11)$$

In Appendix A, we derive the explicit forms of the components $A_{ab}{}^{cd}$, etc. for the 4∂ST EOMs. For the remainder of this paper we will restrict our attention to the particular case of shift-symmetric ESGB gravity.

III. NUMERICAL IMPLEMENTATION

In this section, we describe our methods for numerically evolving the equations of shift-symmetric ESGB gravity, which we recall is a special case of 4∂ST gravity with $V(\phi) = \alpha = 0$ and $\beta = \lambda\phi$. Our general strategy is to, where possible, adapt the methods of Ref. [36] for evolving Einstein gravity in a generalized harmonic formulation to these new equations.

A. Form of equations of motion and gauge choices

We directly evolve the 22 variables (after accounting for the symmetry of the metric components) $\{g_{ab}, \partial_0 g_{ab}, \phi, \partial_0\phi\}$ using the EOM given by Eq. (11).

In addition to the physical metric, we must also specify the auxiliary metrics $\tilde{g}^{ab}$ and $\hat{g}^{ab}$. In general, there is a large degree of freedom in choosing these as functions of g_{ab} and the spacetime coordinates, though here we restrict to a relatively simple choice given by

$$\tilde{g}^{ab} = g^{ab} - \tilde{A}n^a n^b, \qquad (12a)$$

$$\hat{g}^{ab} = g^{ab} - \hat{A}n^a n^b, \qquad (12b)$$

where n^a is the (timelike) unit normal vector to the spacelike hypersurfaces we evolve on, and $\tilde{A}$ and $\hat{A}$ are constants. We emphasize that the MGH formulation only requires $\tilde{g}^{ab}$ and $\hat{g}^{ab}$ to be Lorentzian. We have chosen the ansatz (12) out of its simplicity to implement, and empirically we find that we are able to numerically solve the ESGB equations of motion using auxiliary metrics of this form.

As in the generalized harmonic formulation, we must also choose the source functions H_a, which, combined with the auxiliary metric, determine the coordinate degrees of freedom. Here we restrict to the damped harmonic gauge [37,38] (including the special case of $H_a = 0$), which has been found to work well for a large number of highly dynamical spacetimes, or fix H_a to be constant in time for some cases where we wish to maintain Kerr-Schild like coordinates.

B. Numerical discretization

The numerical scheme we use follows that of Ref. [39]. We discretize the partial differential equations in space, using standard fourth-order finite difference stencils, and in time, using fourth-order Runge-Kutta integration. We implement the EOM directly in the form given by Eq. (11), and invert the set of linear equations at each point using Gaussian elimination. We control high frequency numerical noise using Kreiss-Oliger dissipation [40]. As indicated in Eq. (2), we also use constraint damping to control the constraint violating modes sourced by truncation error. We typically set $\kappa = -1/M_{\rm BH}$, where $M_{\rm BH}$ is the mass of the smallest black hole in the simulation, and

$\rho = 0$, which are similar values to those used in black hole evolutions using the generalized harmonic formulation [41].

As detailed in Ref. [36], we use compactified coordinates so that physical boundary conditions (namely that the metric is flat and the scalar field vanishes) can be placed at spatial infinity. We use Berger-Oliger [42] style adaptive mesh refinement (AMR) supported by the PAMR library [43,44]. The interpolation in time for the AMR boundaries is only third-order accurate, which can reduce the overall convergence to this order in some instances. In some of the cases here, we restrict to axisymmetric spacetimes, and use the modified Cartoon method to reduce our computational domain to a two-dimensional Cartesian half-plane [36].

C. Excision

A crucial ingredient in our ability to evolve black hole spacetimes is the use of excision. In ESGB, the situation is worse than in GR since, as shown in Ref. [27], elliptic regions can develop just inside a black hole horizon, where the EOMs are no longer well-posed, despite the region having bounded curvature. Following Ref. [36], we dynamically track any apparent horizons in our spacetime and excise an interior region. This is done by finding an ellipsoid that just fits inside the apparent horizon and shrinking the axes, typically by 15% to 25%, to create a buffer region between the apparent horizon and the excision surface. In general, we find that we must use smaller excision buffers as the coefficient of the modified gravity terms (i.e. λ) is increased, which requires higher resolution, in order to avoid instabilities near the excision surface.

As the apparent horizon evolves, points that were previously excised may become unexcised and need to be "repopulated" by extrapolating their values from neighboring points. When evolving with unmodified GR equations, this is often done with simple first-order extrapolation, i.e. by taking the average value of the neighboring unexcised points, to avoid high frequency noise (and since the points should initially be out of causal contact with the exterior domain). However, we find that when evolving with ESGB we must use second-order or higher extrapolation, which we speculate is due to the presence of terms of the form $(\partial\partial g)^2$ and $(\partial\partial g)(\partial\partial\phi)$ in the EOM, which are sensitive to jumps in the second derivative. We note that a possible alternative to the excision method used here is to modify the EOMs inside black hole horizons—e.g. by letting the non-GR coupling go to zero—so that they remain hyperbolic [19].

D. Initial data

On our initial data surface, we must satisfy the generalizations of the Hamiltonian constraint $\mathcal{H} \equiv n^a n^b \mathcal{E}_{ab}^{(g)}$ and momentum constraint $\mathcal{M}_\gamma \equiv n^a E_{a\gamma}^{(g)}$, which for 4$\partial$ST gravity take the form,

$$\begin{aligned} \mathcal{H} = &\, n^a n^b R_{ab} + \frac{1}{2}R - (n^a \nabla_a \phi)^2 + X - V(\phi) \\ &- 2\alpha(\phi)X(n^a\nabla_a\phi)^2 + \alpha(\phi)X^2 \\ &+ 2n^a n^b \delta_{ijg(a}^{efcd} g_{b)d} R^{ij}{}_{ef} \nabla^g \nabla_c \beta(\phi) \end{aligned} \tag{13a}$$

$$\begin{aligned} \mathcal{M}_\gamma = &\, n^a R_{a\gamma} - n^a \nabla_a \phi \nabla_\gamma \phi - 2\alpha(\phi)X n^a \nabla_a \phi \nabla_\gamma \phi \\ &+ 2n^a \delta_{ijg(a}^{efcd} g_{\gamma)d} R^{ij}{}_{ef} \nabla^g \nabla_c \beta(\phi). \end{aligned} \tag{13b}$$

Here, we do not implement a method to solve these equations for general ϕ. Instead, we consider initial data for which $\phi = \partial_0 \phi = 0$ on the initial data surface. With this choice of ϕ the ESGB contributions to the constraint equations, which we define to be

$$\mathcal{H}^{(GB)} \equiv 2n^a n^b \delta_{ijg(a}^{efcd} g_{b)d} R^{ij}{}_{ef} g^{gk} \partial_k \partial_c \beta(\phi) \tag{14a}$$

$$\mathcal{M}_\gamma^{(GB)} \equiv 2n^a \delta_{ijg(a}^{efcd} g_{\gamma)d} R^{ij}{}_{ef} g^{gk} \partial_k \partial_c \beta(\phi), \tag{14b}$$

are identically zero on the initial data surface. To show this, we first expand Eqs. (14), imposing $\phi = \partial_0 \phi = 0$ (which implies, e.g. $\partial_a \partial_0 \phi = 0$), rewriting terms to include the unit normal to slices of constant time: $n_a = (-N, 0, 0, 0)$ (here $N = 1/\sqrt{-g^{tt}}$ is the lapse function) so that we are left with

$$\mathcal{H}^{(GB)} = 2\left(-\frac{1}{N}\right) n^a n^b n^g n_q \delta_{ijg(a}^{efqd} g_{b)d} R^{ij}{}_{ef} \beta'(\phi) \partial_0^2 \phi, \tag{15a}$$

$$\mathcal{M}_\gamma^{(GB)} = 2\left(-\frac{1}{N}\right) n^a n^g n_q \delta_{ijg(a}^{efqd} g_{\gamma)d} R^{ij}{}_{ef} \beta'(\phi) \partial_0^2 \phi. \tag{15b}$$

We see that the n^a vectors symmetrize the totally antisymmetric indices of the generalized Kronecker delta; e.g. $n^a n^g \delta_{ijga}^{efcd} = 0$, so that the ESGB contributions to the constraints equations on the initial data surface vanish.

Thus, in shift-symmetric ESGB gravity ($\alpha = V = 0$, $\beta = \lambda\phi$), and with scalar field initial data $\phi = \partial_0 \phi = 0$, the constraint equations on our initial data surface reduce to those of vacuum GR. For cases with a single black hole, we use either harmonic [45,46] coordinates, or Kerr-Schild [47] coordinates (which we discuss in more detail in Sec. IV B). For constructing binary black hole initial data, we solve the Einstein constraints using the conformal thin sandwich solver described in Ref. [48].

Given a particular choice of H^a, we need to ensure that the MGH condition, Eq. (1), is satisfied on the initial data surface. Given initial data $\{g_{ab}, \partial_0 g_{\alpha\beta}\}$ [and hence $\hat{g}_{ab}$ and $\tilde{g}_{ab}$, see Eq. (12)] that satisfy the constraints, we can always do this by solving Eq. (1) for $\partial_0 g_{0a}$. In the language of the $3 + 1$ decomposition, the choice of H^c sets the initial time derivative of the lapse function and shift vector.

E. Diagnostic quantities

In order to characterize our results, we will make use of several diagnostic quantities. Considering first just the canonical coupling of the scalar field to gravity, we can define a stress-energy,

$$T_{ab}^{\mathrm{SF}} \equiv \frac{1}{8\pi}\left(\nabla_a\phi\nabla_b\phi - \frac{1}{2}g_{ab}\nabla_c\phi\nabla^c\phi\right), \qquad (16)$$

although note that when $\lambda \neq 0$ this stress-energy is not generically conserved, $\nabla^a T_{ab}^{\mathrm{SF}} \neq 0$. We can also define an effective stress energy tensor that is conserved, simply by computing the Einstein tensor of the solution,

$$T_{ab}^{\mathrm{Ein}} \equiv \frac{1}{8\pi}\left(R_{ab} - \frac{1}{2}Rg_{ab}\right), \qquad (17)$$

which would be equal to T_{ab}^{SF} in the case that $\lambda = 0$. From T_{ab}^{SF} and T_{ab}^{Ein}, we can define effective energies and energy densities,

$$E \equiv \int t^a n^b T_{ab}\sqrt{\gamma}d^3x \equiv \int \rho_E\sqrt{\gamma}d^3x, \qquad (18)$$

and angular momenta and associated densities,

$$J \equiv \int \hat{\phi}^a n^b T_{ab}\sqrt{\gamma}d^3x \equiv \int \rho_J\sqrt{\gamma}d^3x, \qquad (19)$$

where t_a and $\hat{\phi}_a$ are, respectively, the vectors pointing in the time and azimuthal directions, which would be Killing vectors in the case that the spacetime is stationary and axisymmetric. We note that in axisymmetry, while ρ_J^{SF} will be identically zero, ρ_J^{Ein} can actually be nonzero. Using these stress-energy tensors, we also define an energy flux through a surface as

$$\dot{E} \equiv \int -Nt^a T_a^i dA_i. \qquad (20)$$

We will mainly be interested in computing this quantity in the wavezone, at some surface at large radii. In that case, we expect $\dot{E}^{\mathrm{Ein}}$ to be the same as $\dot{E}^{\mathrm{SF}}$, due to the faster fall-off of the other curvature terms in the wavezone.

During the evolutions, we track any apparent horizons present at a given time and compute several diagnostic quantities with respect to them. From the area of the apparent horizon, we can define an areal mass $M_A \equiv \sqrt{A/(16\pi)}$. In a different context, this would be called the irreducible mass. However, the spacetimes that we study here do violate the null convergence condition (which states that $R_{ab}k^ak^b \geq 0$ for all null k^a), and thus there will be cases where M_A decreases. We

can also associate an angular momentum to the apparent horizon,[5]

$$J_{\mathrm{AH}} \equiv \frac{1}{8\pi}\int \hat{\phi}_i K^{ij}dA_j, \qquad (21)$$

and using the Christodoulou formula, a mass,

$$M_{\mathrm{AH}} \equiv \left(M_A^2 + \frac{J_{\mathrm{AH}}^2}{4M_A^2}\right)^{1/2}. \qquad (22)$$

As an indication of the scalar hair formation about the black hole, we also keep track of the area averaged value of the scalar field on the apparent horizon $\langle\phi\rangle_{\mathrm{AH}}$. In order to compute the gravitational radiation, we extract the Newman-Penrose scalar ψ_4.

IV. RESULTS

A. Hyperbolicity tests with weak field data

As a first test, we consider a weak field configuration and provide numerical evidence that the equations of motion for shift-symmetric ESGB gravity are strongly hyperbolic in the MGH formulation, with the gauge choices we have made. A necessary condition for ESGB gravity to have a well-posed initial value problem is for the equations of motion to have a strongly hyperbolic formulation (e.g. [50]). Papallo and Reall [51,52] have shown that in the generalized harmonic formulation, the EOMs for ESGB gravity are not strongly hyperbolic around generic weak field solutions, instead they are only weakly hyperbolic. Later, Kovacs and Reall showed that the equations of motion for ESGB gravity are strongly hyperbolic in the MGH formulation [17], for weak coupling backgrounds where all the characteristic length scales (associated with the spacetime curvature and scalar gradients) satisfy $L \gg \sqrt{\lambda}$.

In general, one expects that a set of nonlinear weakly (but not strongly) hyperbolic equations of motion will have modes that exhibit frequency dependent growth, where the growth rate increases as a polynomial in the frequency. Given this, we expect that simulations of ESGB gravity in a generalized harmonic formulation should generally not converge with higher resolution, since the higher resolution will resolve smaller scales, and thus allow faster growing fluctuations. This being said, with sufficiently smooth initial data (in particular without AMR, moving excision surfaces, etc., which tend to introduce high frequency numerical error), at a given *fixed* resolution, it may be difficult to observe small scale growth over a finite simulation run time, and one must use nonsmooth initial data in order to make this problem apparent (see e.g. [53] and references therein). This is the approach we take here.

---

[5]We recall that this quantity is conserved if $\hat{\phi}_i$ is tangent to a Killing vector field, regardless of whether the Einstein equations hold, or if the spacetime obeys any energy conditions [49].

Usually, hyperbolicity or robustness tests in GR are performed around Minkowski space or other trivial, scale free background solutions. However, the analysis in Ref. [52] indicates that a "generic" background solution that violates strong hyperbolicity for the generalized harmonic formulation requires nonvanishing derivatives of the scalar field. Therefore, we must resolve a hierarchy of scales given by $L \gg \sqrt{\lambda} \gg \omega^{-1}$, where L is the characteristic length scale of the background curvature, and ω is the frequency of the modes which may violate strong hyperbolicity.[6] In order to make reaching these high resolutions tractable, we impose a translational symmetry in the z direction and restrict to a two-dimensional, periodic domain of length L. The initial data we consider are as follows. For the scalar field we set

$$\phi(t = 0) = \bar{\phi}\sin(2\pi x/L)\sin(2\pi y/L),$$
$$\partial_0\phi(t = 0) = 0, \qquad (23)$$

where here we take the amplitude to be $\bar{\phi} = 0.01$. We set the metric to be initially Minkowski, but add a small white noise perturbation to the initial metric time derivative,

$$g_{ab}(t = 0) = \eta_{ab}, \qquad \partial_0 g_{ab}(t = 0) = f\mathcal{N}/L. \quad (24)$$

Here $\mathcal{N}$ gives a random number between -1 and 1 at every spatial point, and f is a constant controlling the amplitude. Even if f were zero, this solution does not satisfy the constraints, though the constraint violation will in some sense be small since $\bar{\phi} \ll 1$, and our goal here is merely to study the hyperbolicity of the free evolution equations.[7] We only perturb $\partial_0 g_{ab}$ to avoid any issues with the evolution equations being second order in g_{ab} (as constructing a first order version would require introducing a new evolution variable constrained to be equal to $\partial_\alpha g_{ab}$). We set $\lambda/L^2 = 0.025$, so that we are in the weak coupling regime.

We consider a sequence of numerical evolutions where we simultaneously increase the resolution for the numerical grid, while decreasing f. In particular, we consider grid spacings $dx = dy = h_i = L/2^{7+i}$ with $i = 0, 1, \ldots, 5$, and scale the white noise amplitude as $f_i = f_0/2^{4i}$ so that it scales in the same manner as the truncation error with our fourth-order scheme. We choose f_0 so that the white noise perturbation is small, but dominates over the truncation

error ($f_0 \approx 5 \times 10^{-6}$). To monitor the subsequent behavior of the high frequency perturbation, we compute the following difference between subsequent resolutions,

$$\|\partial_0 g_{ab}^h\| = \sum_{ab}\left[\sum_{x,y}(\partial_0 g_{ab}^h - \partial_0 g_{ab}^{h/2})^2\right]^{1/2}, \quad (25)$$

where $\partial_0 g_{ab}^h$ is the numerical solution computed with grid spacing h, the outer sum is a sum over the ten unique metric time derivatives, and the inner sum is a sum over the points in the x and y directions (restricted to a coarse grid of points shared by all resolutions).

We restrict to a gauge with $H^a = 0$, but consider three different choices for the auxiliary metrics corresponding to Eq. (12) with $(\tilde{A}, \hat{A}) = (0, 0)$ (harmonic gauge), $(\tilde{A}, \hat{A}) = (0.1, 0.2)$, and $(\tilde{A}, \hat{A}) = (0.2, 0.4)$. We show the results for these cases in Fig. 1. When the auxiliary metrics are set equal to the physical metric, we do indeed find a perturbation that grows faster and faster as the grid spacing, and hence the minimum wavelength of the perturbation, is decreased. Changing the light cones for the auxiliary metrics by using nonzero $(\tilde{A}, \hat{A})$ improves this, and for $(\tilde{A}, \hat{A}) = (0.2, 0.4)$ there is no evidence of frequency dependent growth.

There is of course no requirement that $\tilde{A}$ and $\hat{A}$ be of some fixed ratio, and in general there is a large degree of freedom in choosing the auxiliary metrics which we do not systematically explore here. For this study, we concentrate merely on finding a choice of parameters that works, and for most of the remaining applications, we will use $(\tilde{A}, \hat{A}) = (0.2, 0.4)$, and rely on convergence tests to estimate the accuracy of our results, and as a check for contamination of the solution due to ill-posedness.

B. Single black hole initial data

We next present simulations where out initial data are a single black hole, restricting to axisymmetry. As discussed in Sec. III D, we begin our evolution in Kerr-Schild coordinates [47]. Our main conclusion in this section is that in full shift-symmetric ESGB gravity (for small enough coupling parameters λ), Kerr initial data lead to stable, rotating, scalar hairy black hole solutions. We note that Kerr solutions for ESGB gravity were evolved using an order-reduction approach in Ref. [34], and stationary solutions to the full theory describing spinning black holes with scalar hair were constructed in Refs. [29,30].

In Fig. 2, we plot the average scalar field value over the black hole apparent horizon $\langle\phi\rangle_{AH}$, along with the change in the black hole mass and spin and the change in black hole mass and spin as measured on the horizon [see Eqs. (21) and (22)], as a function of evolution time t, for different initial (dimensionless) black hole spin parameters a_0, given a fixed value of $\lambda/M^2 = 0.07$ (where M is the Arnowitt-Deser-Misner (ADM) mass). For a given

---

[6]We recall that we need $L \gg \sqrt{\lambda}$, as we are considering hyperbolicity in the weak field regime—in the strong field regime it is likely the theory is not even weakly hyperbolic [27,54].

[7]Moreover we note that, the hyperbolicity analysis of Horndeski gravity theories in generalized harmonic formulations in Refs. [51,52] indicate that the weakly hyperbolic modes were constraint violating ones; thus we expect that the differences between simulations in the MGH and generalized harmonic formulations will be most apparent when we begin with initial data which slightly violate the constraint equations.
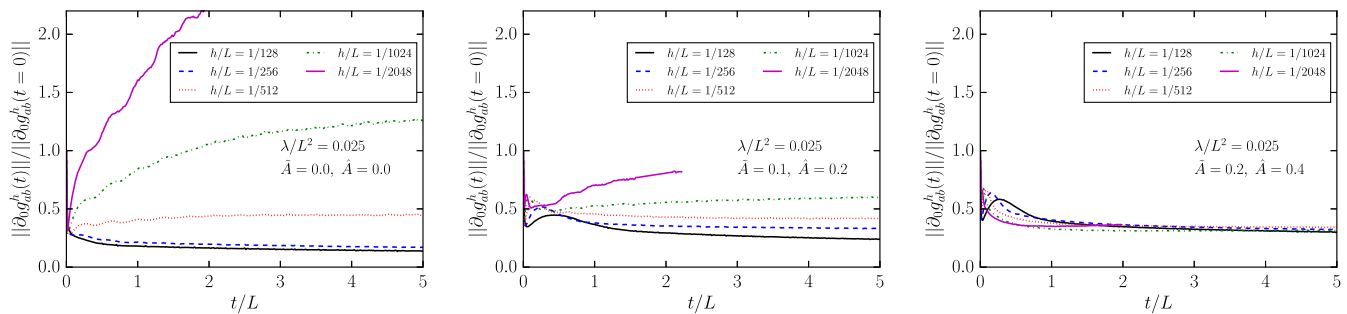
FIG. 1. We show the difference in the evolution variables $\partial_0 g_{ab}$ between subsequent resolutions, computed using Eq. (25), and normalized by the initial value of the white noise perturbation, as a function of time, for a periodic scalar field configuration. The three cases correspond to different choices of the auxiliary metrics in MGH with (left to right) $(\tilde{A}, \hat{A}) = (0, 0)$, $(0.1, 0.2)$, and $(0.2, 0.4)$. In the first case, corresponding to harmonic gauge, frequency dependent growth can be clearly seen as higher frequencies perturbations are sourced for the higher resolutions. With auxiliary metrics that differ sufficiently from the physical one, as in the rightmost panel, this problem no longer appears. Note that the $h/L = 1/4096$ resolution run (needed to compute the error of the $h/L = 1/2048$ run) was continued for a shorter time compared to the lower resolutions due to computational expense.

black hole spin, Ref. [29] found that there is a maximum λ/M^2 above which they could no longer construct regular solutions to the theory, and this maximum decreased with increasing spin. For a spin parameter of $a = 0.9$, the coupling limit was found to be $\lambda/M^2 \approx 0.13$, while for $a = 0.99$, it was found to be roughly a factor of 2 smaller [29]. We find it difficult to consider couplings near this limit for a given spin, which we believe is in part due to the fact that the scalar hair initially exceeds its stationary value during the growth of the scalar cloud before settling down to a lower value (e.g. the top left panel of Fig. 2; see also [28]), so that any problems that could occur from, e.g. loss of hyperbolicity come closer to the horizon than one would anticipate from studies of stationary solutions. But we have not explored extensively whether better choices of gauge and auxiliary metrics could also improve this.

We find that the average asymptotic scalar field value at the horizon decreases as a function of initial dimensionless Kerr spin parameter. This is consistent with the fact that the average value of the Gauss-Bonnet scalar is a decreasing function of black hole spin; in fact, at a critical value of $a \gtrsim 0.766$, the average value of the Gauss-Bonnet scalar is negative on the black hole horizon. We find that the average value of the scalar field only becomes negative for larger spins ($a \gtrsim 0.95$), which is most likely due to the fact that stationary scalar field configurations must balance gradients with the varying Gauss-Bonnet source term on the horizon. We find that as we increase the black hole spin, the scalar field becomes negative on the spin axis (where the Gauss-Bonnet scalar is negative) but remains positive on the equator of the black hole (where the Gauss-Bonnet scalar is positive). The formation of scalar hair decreases both the mass and angular momentum of (as measured on the horizon) the initial spinning black hole. However, from Fig. 2, we can see

that for initial black hole spins that are roughly less than $a_0 \lesssim 0.7$, black hole scalar hair formation increases the dimensionless spin, while for greater initial black hole spins, it decreases the dimensionless spin somewhat. For initial black hole spin $a = 0.9$ and $\lambda/M^2 = 0.07$, we see that the change in the dimensionless black hole spin is approximately $\sim -2\%$ while the change in the black hole mass is approximately $\sim -2\%$.

In Fig. 3, we show a convergence study of the average scalar hair profile, along with the change of the black hole angular momentum and mass [see Eqs. (21) and (22)] as measured on the horizon of a black hole with initial dimensionless spin parameter of $a_0 = 0.99$. We see that the change in the black hole horizon angular momentum is $\sim 0.2\%$, while the change in the black hole mass is $\sim 0.8\%$. In this study, the integrated constraint violation C^a converges at third order, (consistent with the time interpolation used by the AMR algorithm). Here, and in subsequent sections, we show $|C^a|$ integrated over the coordinate radius $r \leq 100\,M$ region of the domain. We found that as we considered larger black hole spins, we could only obtain stable, convergent evolution with small ESGB couplings, and had to place our excision radius closer to the black hole horizon. Figure 4 shows a snapshot of the scalar field around a black hole with initial spin $a = 0.99$, taken after $150M$ of evolution. The scalar field is positive around the equator of the black hole, while it is negative around the spin axis.

One reason to expect that only smaller Gauss-Bonnet couplings can be used to evolve higher spin black holes is because the Kerr ring curvature singularity moves closer to the black hole horizon for larger spins, and there is numerical evidence that the equations of motion for ESGB gravity are hyperbolic only for regions of relatively small curvature (given a fixed Gauss-Bonnet coupling) [27,28,54].
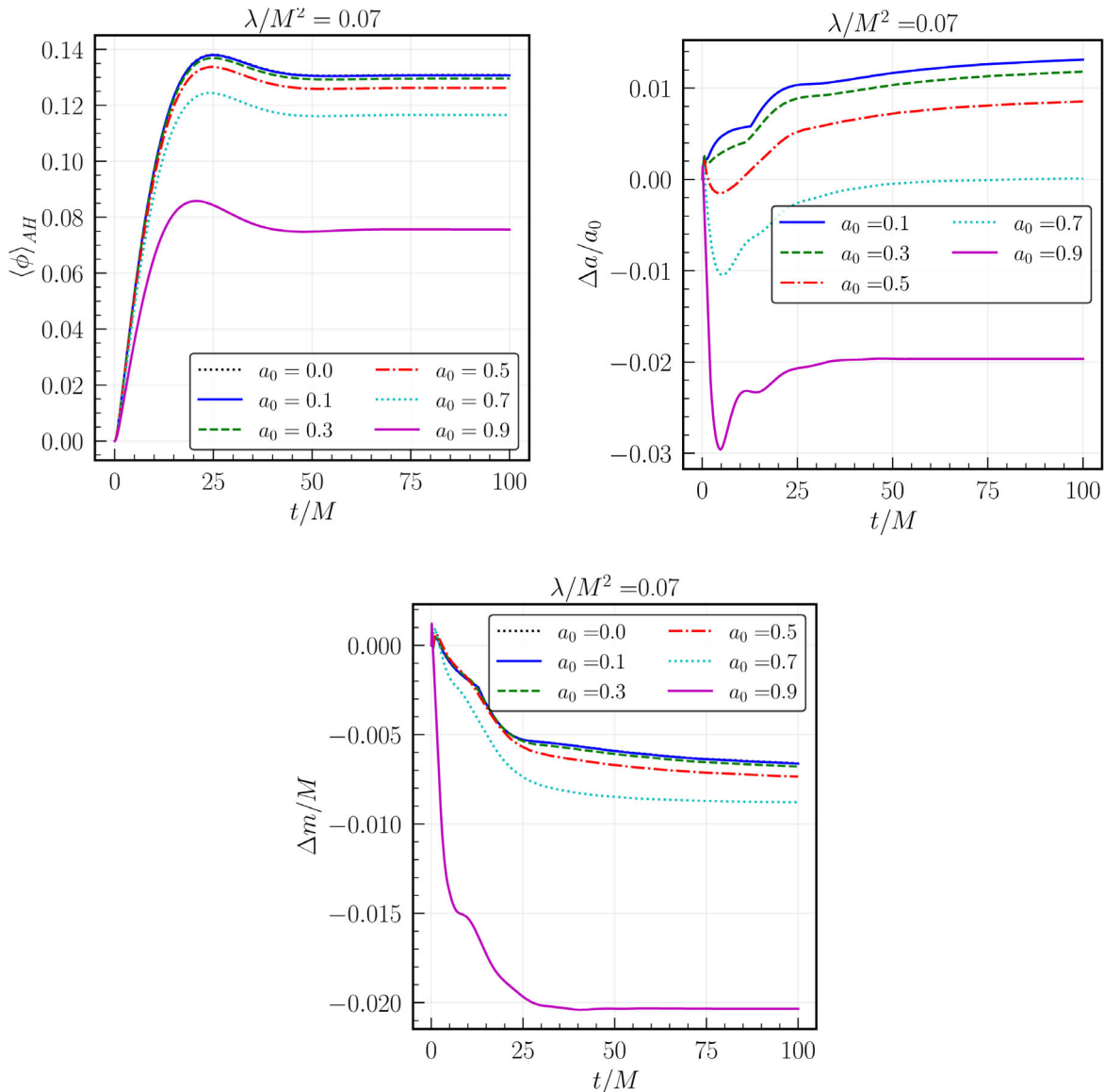
FIG. 2. Left to right: The horizon-averaged scalar field $\langle \phi \rangle_{AH}$, value of dimensionless black hole spin (normalized by the initial black hole spin a_0), and value of black hole mass m (normalized by the ADM mass M), for a one-parameter family of Kerr initial data. We show the scalar cloud profile on the black hole horizon for $\lambda/M^2 = 0.07$ (runs with $\lambda/M^2 = -0.07$ give qualitatively similar results, except $\langle \phi \rangle_{AH}$ has the opposite sign). Though the black hole always loses angular momentum as a result of scalar hair growth, from the center panel we see that for small enough black hole spins ($a \lesssim 0.7$), the dimensionless spin decreases, while for larger spins it increases (for the case $a_0 = 0$, the black hole spin does not change, so we omit it from this figure). The growth of the scalar cloud always coincides with a decrease in the mass of the black hole, which we interpret as the scalar field extracting energy from the black hole.

C. Head-on binary black hole mergers

We next study binary black hole mergers in ESGB. We begin by restricting to the axisymmetric case of a head-on collision, which allows us to quickly cover a number of different parameters, including different values of λ, as well as different black hole spins and mass ratios. Since the corrections in ESGB are sensitive to the smallest length scale, we will label the cases we consider in terms of the quantity λ/m^2, where m is the mass of the smallest black hole in the initial data.

Our main result in this section is that we find that the ESGB theory in general, and the MGH formulation in particular, remains hyperbolic, even in the highly dynamical setting of a (head-on) binary black hole merger, for comparable values of λ to where the spherically symmetric problem remains well posed. For reference, in Ref. [28], the maximum value where the scalar hair grew about a Schwarzschild black hole that could be evolved without the loss of hyperbolicity was $\lambda/m^2 \approx 0.19$, and based on extrapolation, it was estimated that hyperbolicity would be lost outside the black horizon for $\lambda/m^2 \gtrsim 0.23$.
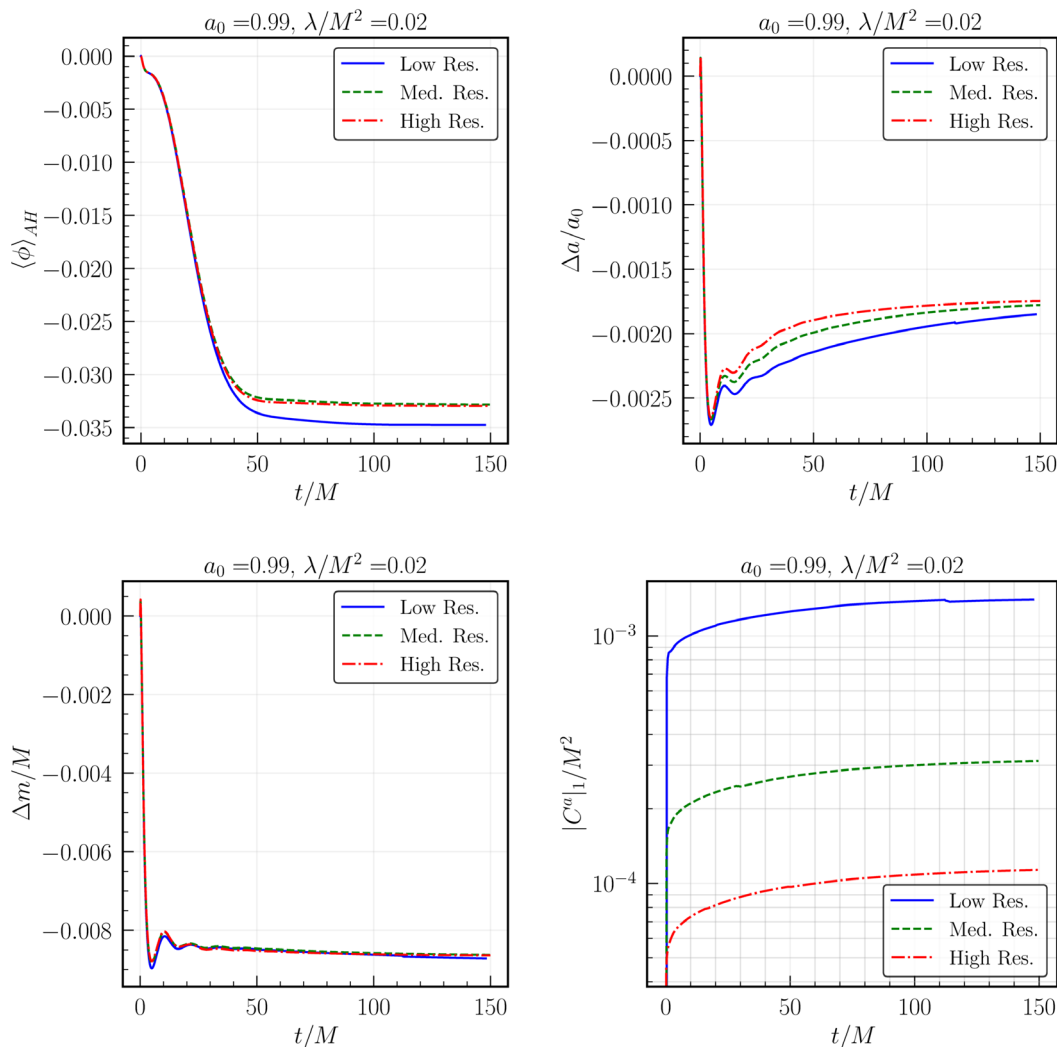
FIG. 3.   Convergence study of the scalar hair growth about a black hole with $a_0 = 0.99$ and $\lambda/M^2 = 0.02$. We show the horizon-averaged scalar field $\langle\phi\rangle_{AH}$ (top right), change in dimensionless black hole spin a (top left), relative change in the black hole mass (bottom right), and constraint violation $|C^a|$ (normalized by the initial black hole mass M; bottom left). We find that the constraint violation converges at third order, as expected. The medium and high resolutions have 1.5 and 2× the linear resolution of the low resolution simulation. For an image of the scalar field density around the black hole, see Fig. 4.

As discussed in Sec. III D, we start with initial data where ϕ and $\partial_0\phi$ are identically zero. Hence, initially the individual black holes will develop scalar hair as they fall towards each other and finally merge. We choose the initial separation of the black holes to be $d = 50M$ (where M it the ADM mass of the spacetime) and set their initial velocities to the value corresponding to the binary being marginally bound. We show a number of cases with an equal-mass, nonspinning binary black hole, and different values of the coupling ranging from $\lambda/m^2 = 0$ to 0.18 in Fig. 5. Initially scalar hair grows about the black hole, which loses mass as the cloud grows. For larger couplings, there is a small increase in the magnitude of ϕ on the horizons as the black holes approach each other (bottom panel of Fig. 5) and a corresponding decrease in black hole mass (top panel). However, when the black holes merge, forming a larger

black hole, the Gauss-Bonnet curvature outside the common horizon becomes smaller, and the scalar cloud shrinks. As elaborated on below, most of the energy lost by the smaller black hole goes back into the remnant black hole, as opposed to escaping as radiation.

In Fig. 6, we show the radiation from the black hole mergers. Increasing λ to larger values slightly decreases the merger time and increases the gravitational radiation. More pronounced is the effect this has on the scalar radiation, which roughly scales as λ^2, though on top of this, some additional nonlinear enhancement is evident for large values. For $\lambda/m^2 \gtrsim 0.1$, the scalar field luminosity is comparable to the gravitational wave luminosity for this configuration.

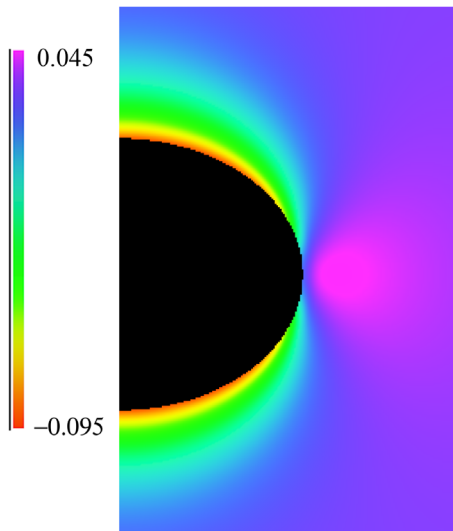Even though these black hole merger spacetimes are far from being stationary, except at late times after the final

FIG. 4. The scalar field value around a black hole of initial dimensionless spin $a_0 = 0.99$ and dimensionless coupling $\lambda/M^2 = 0.02$, taken after $150M$ of evolution. For the evolution of the black hole parameters, see Fig. 3. The spacetime is axisymmetric, and we show a slice at fixed azimuthal angle, with the bottom of the figure corresponding to the axis of symmetry. The excised region within the apparent horizon, which is roughly 90% of the radius of the black hole, is shown in black. The colorbar indicates the scalar field value, which in this case varies between $\phi \in [-0.095, 0.045]$. We see that on the equator of the spinning black hole (middle of the figure), the scalar field is positive, while at the poles, the scalar field is negative. This is to be contrasted with black holes with zero spin and $\lambda > 0$, where ϕ is everywhere positive.
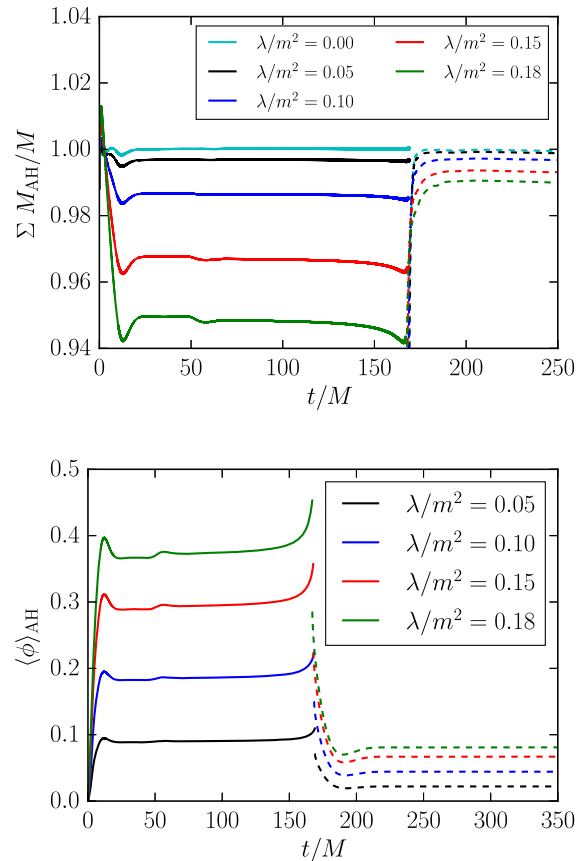

FIG. 5. Top: The sum of the masses of the merging black holes (solid lines) or mass of the final black hole (dashed lines) as a function of time for head-on mergers of equal mass, nonspinning black holes and different values of λ. Bottom: The area-averaged value of ϕ on the apparent horizon as a function of time.

remnant has settled down, it is still instructive to study an approximate measure of how energy is distributed as a function of time. In Fig. 7, we show this for a stronger coupling case with $\lambda/m^2 = 0.15$. We can see that as the black holes form scalar hair and as their mass decreases, there is a comparable increase in the effective energy calculated from the Einstein tensor E^{Ein}, with roughly half of this being attributable to the canonical scalar field energy E^{SF}. After the formation of a common horizon, these quantities rapidly decrease. For this case, most of energy that does not end up in the final black hole is actually radiated away as scalar radiation (dotted green curve in Fig. 7). In fact, the initial scalar hair growth of the individual black holes produces stronger radiation than the merger.

We also show the integrated norm of the constraint violation [Eq. (1)] for $\lambda/m^2 = 0.15$ and several resolutions in Fig. 8, demonstrating that this quantity is converging to zero at the expected rate. Here the lowest resolution has a grid spacing of $dx \approx 0.02M$ on the finest level, and the highest resolution is twice as high.

To probe the effect of angular momentum, we also study mergers of spinning black holes. We consider two axisymmetric configurations where the magnitude of the dimensionless black hole spin is $|a| = 0.6$: one where the spins are aligned, and one where they are antialigned. In Fig. 9, we show how the angular momentum evolves in the aligned cases. Initially, as the black holes grow scalar hair, angular momentum moves from the black hole horizons to the scalar clouds. As the black holes merge, most of this angular momentum goes back into the final black hole.

The scalar radiation produced by the spinning black hole mergers is slightly smaller compared to the nonspinning cases, as shown in the top panel of Fig. 10. We also find that the differences between the aligned and antialigned spins is negligible for these cases. We note that in axisymmetry, the scalar field radiation does not carry angular momentum.

Finally, we consider a 4∶1 mass-ratio merger of nonspinning black holes. In this configuration, the smaller black hole will have more scalar hair than the larger one, which tends to suppress nonlinear effects in the coupling due to the merger. In the bottom panel of Fig. 10, we show the scalar radiation from two cases with $\lambda/m^2 = 0.05$ and
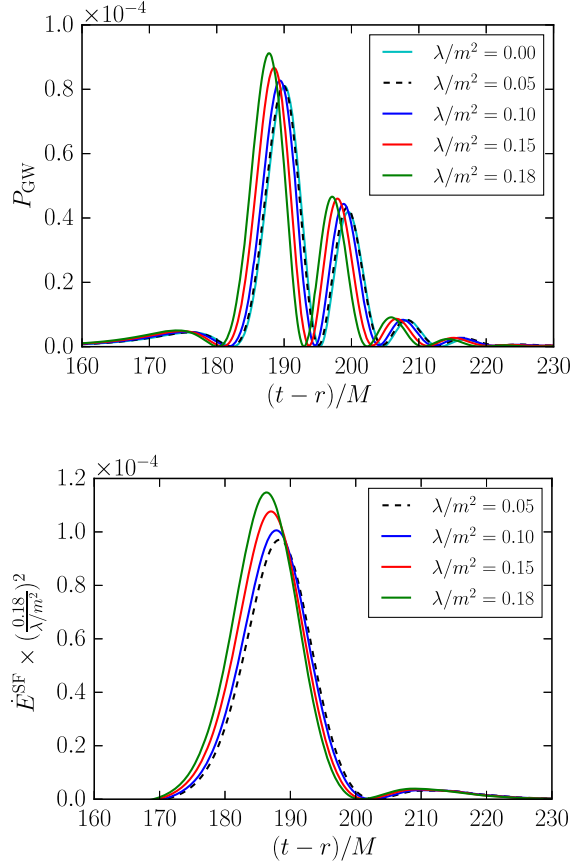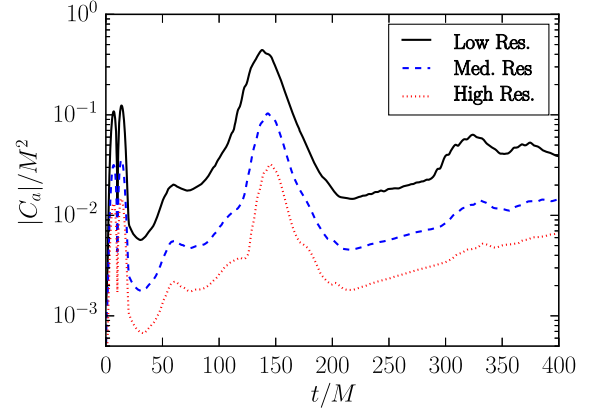
FIG. 8. Integrated norm of the constraint violation [Eq. (1)] as a function of time (in units of total mass) for an equal-mass binary black hole merger with $\lambda/m^2 = 0.15$ at three resolutions. The medium and high resolutions have 1.5 and 2× the linear resolution of the low resolution simulation.

0.1. Compared to the equal-mass cases, the luminosity is smaller by roughly a factor of ~12. After rescaling by λ^2, the $\lambda/m^2 = 0.05$ and 0.1 cases are indistinguishable for a 4:1 mass ratio.

D. 3D results: Scalar hair formation about a boosted, spinning black hole

We next discuss results for spinning, boosted black hole initial data. To consider a fully 3D example, we choose the initial spin axis and boost axis to be unaligned—e.g. the initial spin of the black hole is in the z direction, and the boost is in the y direction. As discussed in Sec. III D, our initial data for the scalar field are $\phi = \partial_0 \phi = 0$, so that we initially start out with a boosted, spinning black hole (in harmonic coordinates), which subsequently forms a scalar

FIG. 6. Top: The gravitational wave luminosity from the head-on collisions of equal-mass, nonspinning black holes with different values of λ. Bottom: The flux of energy radiated away in the scalar field for the same cases. The different cases have been scaled to the highest value of λ assuming λ^2 scaling.
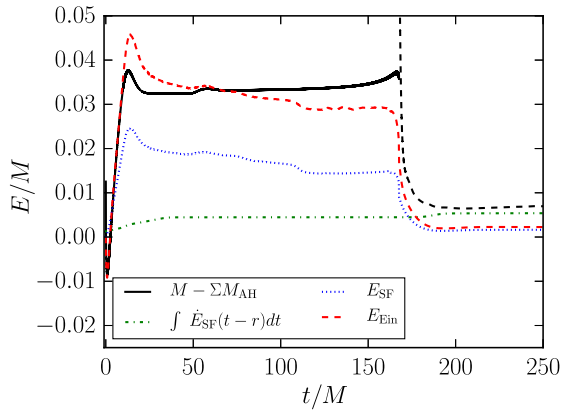
FIG. 7. Various measures of energy as a function of time for a head-on collisions of equal-mass, nonspinning black holes with $\lambda/m^2 = 0.15$. We show the difference of the total mass from the sum of the mass of the apparent horizons, the scalar field energy radiated away (at $r = 50M$), the integrated energy in the canonical scalar field component E^{SF}, and calculated from the Einstein tensor E^{Ein}. We note that the last two quantities are gauge dependent except when the spacetime is stationary, which approximately holds at late times.
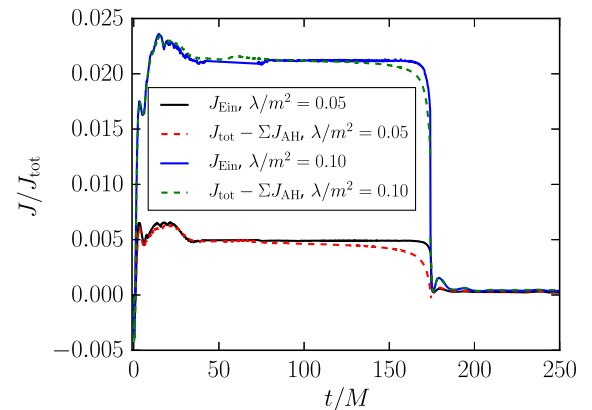

FIG. 9. Angular momentum as a function of time for a head-on collisions of equal-mass black holes with aligned $a = 0.6$ spins and $\lambda/m^2 = 0.05$ and 0.1. We show the difference of the total angular momentum from the sum of the angular momentum of the apparent horizons and the integrated angular momentum calculated from the Einstein tensor J_{Ein}.
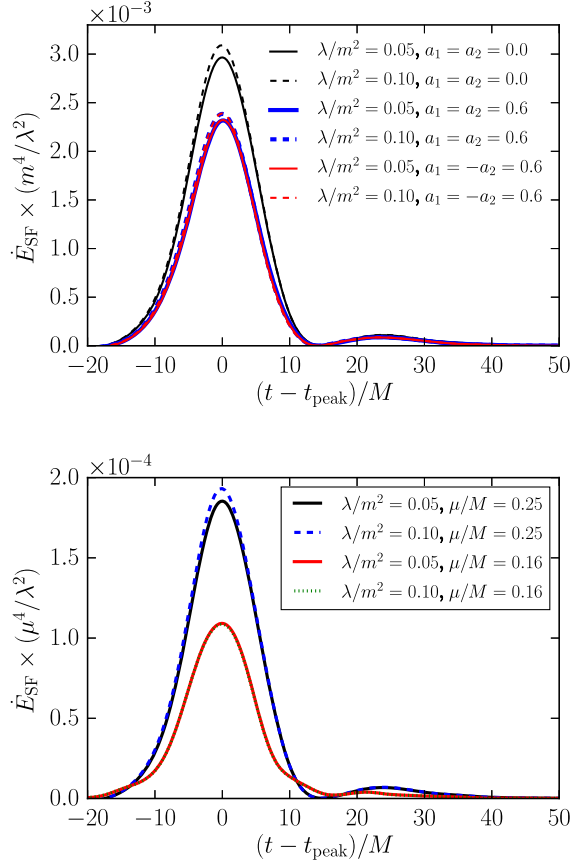
FIG. 10. The scalar luminosity in the wavezone ($r/M = 100$) for various head-on black hole mergers. Top: A comparison of different values of black hole spin and ESGB coupling for equal mass mergers. The luminosity has been scaled assuming a λ^2 dependence. Bottom: A comparison of different values of mass-ratio and coupling for nonspinning mergers. The luminosity has been scaled by λ^2/μ^4, where μ is the reduced mass of the binary.
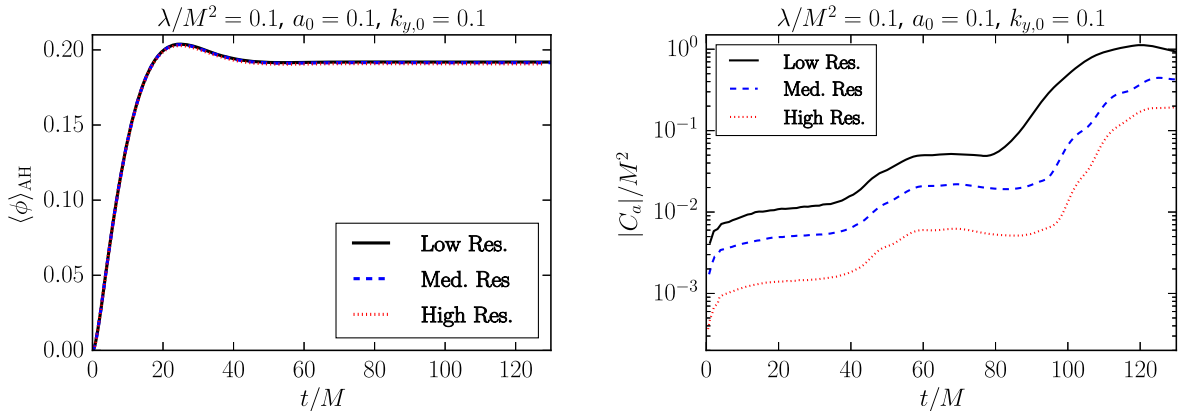
cloud. Therefore, unlike in the vacuum Einstein equations case, the black hole boost is more than just a coordinate transformation. The main result of this section is that the boosted, spinning black hole spontaneously form scalar hair and that we obtain stable, convergent evolution.

We show one example case in this section: a Kerr black hole with initial dimensionless spin $a = 0.4$, and with a boost $k_{y,0} = 0.1$ (i.e. at 10% the speed of light) orthogonal to the initial spin axis. (We found similar results for other cases with higher spins and lower values of coupling, e.g. $a = 0.2$ and $\lambda/M^2 = 0.05$.) In Fig. 11, we show a convergence study of the constraint violation $|C^a|$ and find third order convergence, with no sign of resolution dependent growth. Our results for the boosted, spinning black hole are qualitatively similar to our simulations of spinning black holes in axisymmetry: a scalar field grows and then settles down to an equilibrium configuration around the black hole, emitting a burst of scalar radiation in the process.

E. 3D results: Binary black hole inspiral and merger

Finally, we consider the inspiral and merger of a binary black hole without continuous symmetries. Here we just present results for one case consisting of an equal-mass, nonspinning binary that undergoes ~3 orbits before merging, and for a relatively small value of the Gauss-Bonnet coupling $\lambda/m^2 = 0.01$ (where again, m refers to the mass of one constituent of the binary), where nonlinear effects are small. As part of the process for constructing initial data, we evolve the binary black hole data obtained from solving the constraint equations for ~$50M$ (where M is the ADM mass) just using the Einstein equations, to reduce the

FIG. 11. Convergence study of the horizon-averaged scalar field $\langle\phi\rangle_{AH}$ (left) and constraint violation $|C_a|$ (normalized by the initial black hole mass M; right), for a fully 3D case with a black hole with initial boost $k_{y,0} = 0.1$, dimensionless spin 0.1, and coupling $\lambda/M^2 = 0.1$. We find that the constraint violation converges at third order. The transient growth at $t \sim 100\,M$ in this quantity is due to the scalar radiation from initial scalar hair growth hitting the outermost mesh refinement level, which leads to some spurious reflection (which converges away). The medium and high resolutions have 1.5 and 2× the linear resolution of the low resolution simulation.

gauge dynamics and spurious high frequency gravitational wave content. We then use this as initial data for the evolution with the full ESGB equations.

As was found for the head-on black hole merger, the black holes rapidly form scalar hair, after which the scalar field around the individual horizons is essentially constant, with a small uptick in the last stages of the merger that is cutoff by the appearance of the common horizon. We show the gravitational and scalar radiation for this system in Fig. 12. As was seen in the head-on black hole mergers, the burst of scalar radiation from the initial growth of the scalar hair about the individual black holes of the binary is actually larger than for the merger. Following this initial transient, the scalar radiation tracks the inspiral of the binary evident in the gravitational waves. As expected from the results in Sec. IV C, at this small value of the coupling the scalar radiation is much smaller than the gravitational radiation. Ignoring the initial burst, which is just an artifact of our initial conditions, $\approx 3 \times 10^{-6} M$ is emitted in scalar radiation during the last few orbits, mostly at
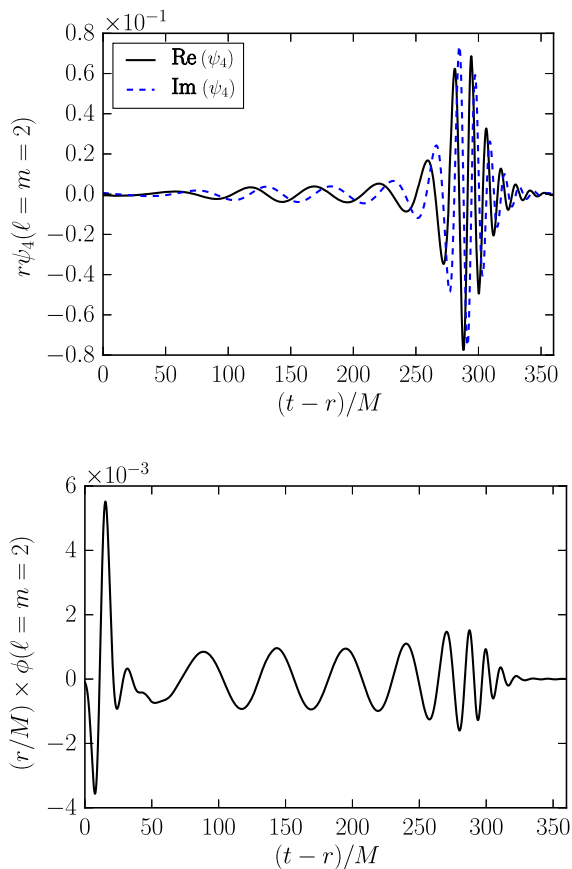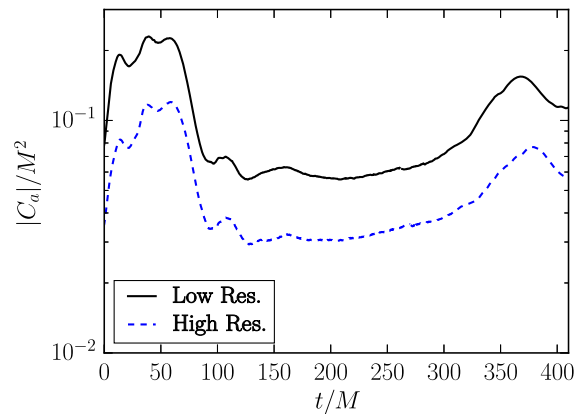

FIG. 13. The integrated norm of the MGH constraint violation $|C_a|$ for the inspiral and merger of an equal-mass binary black hole with $\lambda/m^2 = 0.01$. The high resolution case has $4/3\times$ the resolution of the low resolution, and the convergence is consistent with third order.

merger (compared to a few percent M emitted in gravitational waves).

We perform this calculation at two different resolutions where the lower resolution has a grid spacing of $dx/M \approx 0.025$ on the finest mesh refinement level, and the higher resolution has $4/3\times$ this resolution. We show the time dependence of the integrated MGH constraint in Fig. 13. This is consistent with third-order convergence and shows no sign of resolution dependent growth.

We present these results primarily to illustrate that these methods work for the binary inspiral problem, at least at sufficiently modest values of the modified gravity coupling. We leave the exploration of higher values of the coupling and different binary configurations, as well as additional resolution studies, to future work.

FIG. 12. The radiation from the inspiral and merger of an equal mass binary black hole with $\lambda/m^2 = 0.01$. Top: The real and imaginary components of the $\ell = m = 2$ spin -2 spherical harmonic of the Newman-Penrose scalar, which encodes the gravitational waves. Bottom: The $\ell = m = 2$ component of the scalar field in the wavezone. The burst at early times comes from the growth of the scalar hair about the individual black holes of the initially vacuum binary.

V. DISCUSSION AND CONCLUSION

In this article we present numerical solutions of dynamical spacetimes in ESGB gravity without any particular symmetry restrictions or approximations. We evolve the shift-symmetric ESGB EOMs using the MGH formulation, for which the theory has a well-posed initial value problem (at least at weak coupling) [16,17]. We are able to solve for the dynamics of single and binary (scalar hairy) black hole spacetimes in this theory, including cases with spinning black holes and binaries with unequal mass-ratios, and in the regime where the formation of scalar hair changes the black hole mass at the level of a few percent, and the scalar radiation becomes comparable to the gravitational radiation. Given the novelty of the modified harmonic formulation, and the dearth of results on the nonlinear dynamics of Horndeski theories in regimes of physical interest, there are many avenues for future research. In this section we outline a few such directions.

Here, we presented one case consisting of a few orbits and merger of a quasicircular binary black hole at a relatively modest value of the Gauss-Bonnet coupling, to demonstrate that our methods work for such configurations. However, based on the results from head-on collisions, higher values of coupling, where nonlinear effects due to the ESGB terms are more important, should be tractable. In future work, we will explore the parameter space of binary black hole mergers more thoroughly, in order to make a better connection to gravitational wave observations, which can be used test such modifications to GR. Here, we have focused on shift-symmetric ESGB, but our methods should be generally applicable both to ESGB with other couplings, and Horndeski gravity theories in general, potentially allowing binary black hole mergers in all these cases to be explored. Direct simulations of the full EOMs could also be compared to various approximate treatments of these theories, including the order reduction approach [13], or modified forms of the EOMs that are designed to improve the hyperbolicity [15], in order to quantify the errors coming from secular or nonperturbative effects in a binary inspiral (such a comparison for a toy scalar-field problem was carried out in Ref. [55]). This would help determine the best methods to use for theories where the short wavelength behavior is not known, and there is not a well-posed initial value problem.

In tackling the above, another future research direction is to better understand the robustness of the MGH formulation, both of the Einstein equations, and of the Horndeski gravity theories, under different gauge choices. In this new formulation, one can freely choose not only the source functions, but also the two auxiliary metrics $\tilde{g}^{ab}$ and $\hat{g}^{ab}$ which determine the light cone of the gauge and constraint propagating modes. Our particular choice of the auxiliary metrics [Eq. (12)] was guided mostly by convenience, and it would be interesting to look for improved choices of auxiliary metrics that could, for example allow us to better evolve black hole spacetimes with larger ESGB coupling. Potential future directions include: considering different ratios of the parameters $\tilde{A}$ and $\hat{A}$, and considering different ansatzes for the auxiliary metrics $\tilde{g}^{ab}$ and $\hat{g}^{ab}$ (for example, it would be considering auxiliary metrics where $\tilde{A}$ and $\hat{A}$ are functions of the spacetime geometry; for more discussion see [17]).

Another research direction is to develop robust initial data solution methods for the Horndeski theories. This will be necessary for numerically constructing initial data for, e.g. inhomogeneous cosmological solutions to Horndeski theories, or binary initial data that do not have a strong initial transient due to, e.g. initial black hole scalar hair formation. The first step in this direction would be to formulate the Horndeski constraints as elliptic equations, for example using a conformal thin-sandwich type approach [56].

Finally, given the number of Horndeski theories that have been invoked in both the early and late Universe (e.g. [57–61]), a natural direction for future research is to consider cosmological solutions to Horndeski theories. Given the failure of GR coupled to ordinary matter to resolve the initial cosmological singularity [62], it would be interesting to determine if *any* classical field theory that had well-posed evolution could resolve this issue in a mathematically satisfactory way, while also obeying current observational and experimental constraints. Potential candidate theories that have been proposed (e.g. bouncing universes [58], or "genesis" [59,63]), fall under the Horndeski class of theories, and thus should be amenable to being solved using a MGH formulation.

APPENDIX A: DERIVATION OF EVOLUTION MATRIX FOR 4∂ST GRAVITY IN A MODIFIED HARMONIC FORMULATION

For completeness, and for reference, here we show our derivation of the components of the evolution matrix, Eq. (11), for the EOMs of 4∂ST gravity, Eqs. (7) and (8).

We find it convenient to split our calculation into several steps: first we rewrite the equations for the Einstein-minimally coupled scalar field contributions to the EOMs, then for the contributions that involve α, and then, finally, for the contributions that involve β.

1. Terms: Einstein, minimally coupled scalar field, and constraint damping

We first consider the Einstein-modified harmonic contribution to the tensor EOMs,

$$R_{ab} - \left(\hat{P}_c{}^d{}_{ab} - \frac{1}{2}g_{ab}\hat{P}_c{}^d\right)\nabla_d C^c$$

$$-\frac{1}{2}\kappa(n_a C_b + n_b C_a - (1+\rho)n_c C^c g_{ab})$$

$$= 8\pi\left(T_{ab} - \frac{1}{2}g_{ab}T\right). \tag{A1}$$

It is straightforward to see that

$$B_{ab} = 0. \tag{A2}$$

We next consider

$$\nabla_d C^c = \nabla_d(H^c + \tilde{g}^{ef}\Gamma^c_{ef})$$

$$= \frac{1}{2}\tilde{g}^{ef}g^{cg}(\partial_d\partial_e g_{gf} + \partial_d\partial_f g_{ge} - \partial_d\partial_g g_{ef})$$

$$+ \tilde{g}^{ef}\partial_d g^{cg}\Gamma_{gef} + \partial_d\tilde{g}^{ef}\Gamma^c_{ef} + \partial_d H^c$$

$$+ \Gamma^c_{dg}(H^g + \tilde{g}^{ef}\Gamma^g_{ef}). \tag{A3}$$

Using

$$R_{ab} = \partial_c\Gamma^c_{ab} - \partial_a\Gamma^c_{cb} + \Gamma^c_{dc}\Gamma^d_{ab} - \Gamma^c_{da}\Gamma^d_{cb}$$

$$= -\frac{1}{2}g^{cd}(\partial_c\partial_d g_{ab} - \partial_c\partial_b g_{ad} - \partial_a\partial_d g_{bc} + \partial_a\partial_b g_{cd})$$

$$+ \partial_c g^{cd}\Gamma_{dab} - \partial_a g^{cd}\Gamma_{dcb} + \Gamma^c_{dc}\Gamma^d_{ab} - \Gamma^c_{da}\Gamma^d_{cb}, \tag{A4a}$$

$$\partial_c g^{cd}\Gamma_{dab} + \Gamma^c_{dc}\Gamma^d_{ab} = -\Gamma_d\Gamma^d_{ab}, \tag{A4b}$$

$$\partial_a g^{cd}\Gamma_{dcb} = \frac{1}{2}\partial_a g^{cd}\partial_b g_{dc}$$

$$= \frac{1}{4}\partial_a g^{cd}\partial_b g_{dc} + \frac{1}{4}\partial_b g^{cd}\partial_a g_{dc}, \tag{A4c}$$

we then have

$$-\frac{1}{2}A_{ab}{}^{cdef}\partial_c\partial_d g_{ef} - \frac{1}{4}\partial_a g^{cd}\partial_b g_{cd} - \frac{1}{4}\partial_b g^{cd}\partial_a g_{cd} - \Gamma_d\Gamma^d_{ab} - \Gamma^c_{da}\Gamma^d_{cb}$$

$$-\left(\hat{P}_c{}^d{}_{ab} - \frac{1}{2}g_{ab}\hat{P}_c{}^d\right)(\partial_d H^c + \Gamma_{gef}\tilde{g}^{ef}\partial_d g^{cg} + \Gamma^c_{ef}\partial_d\tilde{g}^{ef} + \Gamma^c_{dg}(H^g + \tilde{g}^{ef}\Gamma^g_{ef}))$$

$$-\frac{1}{2}\kappa(n_a C_b + n_b C_a - (1+\rho)n_c C^c g_{ab}) = 8\pi\left(T_{ab} - \frac{1}{2}T g_{ab}\right), \tag{A5}$$

where

$$A_{ab}{}^{cdef} \equiv \delta_a^e\delta_b^f g^{cd} - \delta_a^f\delta_b^d g^{ce} - \delta_a^c\delta_b^f g^{de} + \delta_a^c\delta_b^d g^{ef} + 2\left(\hat{P}^{ec}{}_{ab} - \frac{1}{2}g_{ab}\hat{P}^{ec}\right)\tilde{g}^{df} - \left(\hat{P}^{dc}{}_{ab} - \frac{1}{2}g_{ab}\hat{P}^{dc}\right)\tilde{g}^{ef}. \tag{A6}$$

Note that we can interchange $c \leftrightarrow d$ and $e \leftrightarrow f$, as partial derivatives commute and g_{ef} is symmetric. We use this fact below to simplify some of the expressions. To see the structure of the principal symbol in more detail we expand out $\hat{P}^{cd}{}_{ab}$,

$$\hat{P}^{dc}{}_{ab} - \frac{1}{2}g_{ab}\hat{P}^{dc} = \frac{1}{2}\left(\delta_a^d\hat{g}_b{}^c + \delta_b^d\hat{g}_a{}^c - g^{cd}\hat{g}_{ab} - g_{ab}\left(\hat{g}^{dc} - \frac{1}{2}g^{cd}\hat{g}\right)\right). \tag{A7}$$

We then have

$$A_{ab}{}^{cdef} = \delta_a^e\delta_b^f g^{cd} - (\delta_a^f\delta_b^d g^{ce} - \delta_a^f\hat{g}_b{}^d\tilde{g}^{ce}) - (\delta_a^c\delta_b^f g^{de} - \delta_b^f\hat{g}_a{}^c\tilde{g}^{de}) + (\delta_a^c\delta_b^d g^{ef} - \delta_{(a}^d\hat{g}_{b)}^c\tilde{g}^{ef})$$

$$-\left(g^{ce}\hat{g}_{ab} + \hat{g}^{ce}g_{ab} - \frac{1}{2}g_{ab}g^{ce}\hat{g}\right)\tilde{g}^{df} + \frac{1}{2}\left(g^{cd}\hat{g}_{ab} + g_{ab}\hat{g}^{cd} - \frac{1}{2}g_{ab}g^{cd}\hat{g}\right)\tilde{g}^{ef}. \tag{A8}$$

From Eq. (A5), we can read off $A_{ab}{}^{cd}$ and $F^{(g)}_{ab}$,

$$A_{ab}{}^{cd} = A_{ab}{}^{00cd}, \tag{A9}$$

$$F_{ab}^{(g)} = A_{ab}{}^{\alpha\beta ef}\partial_\alpha\partial_\beta g_{ef} + 2A_{ab}{}^{(\alpha 0)ef}\partial_\alpha\partial_0 g_{ef} - \frac{1}{4}\partial_a g^{cd}\partial_b g_{cd} - \frac{1}{4}\partial_b g^{cd}\partial_a g_{cd} - \Gamma_d\Gamma_{ab}^d - \Gamma_{da}^c\Gamma_{cb}^d$$

$$- \left(\hat{P}_c{}^d{}_{ab} - \frac{1}{2}g_{ab}\hat{P}_c{}^d\right)(\partial_d H^c + \Gamma_{gef}\tilde{g}^{ef}\partial_d g^{cg} + \Gamma_{ef}^c\partial_d\tilde{g}^{ef} + \Gamma_{dg}^c(H^g + \tilde{g}^{ef}\Gamma_{ef}^g))$$

$$- \frac{1}{2}\kappa(n_a C_b + n_b C_a - (1+\rho)n_c C^c g_{ab}) - 8\pi\left(T_{ab} - \frac{1}{2}Tg_{ab}\right), \tag{A10}$$

The contribution of the scalar field is

$$F_{ab}^{(g)} = -\nabla_a\phi\nabla_b\phi - V(\phi)g_{ab}, \tag{A11}$$

$$D = g^{00}, \tag{A12}$$

$$F^{(\phi)} = g^{\alpha\beta}\partial_\alpha\partial_\beta\phi + 2g^{\alpha 0}\partial_\alpha\partial_0\phi - g^{ab}\Gamma_{ab}^c\partial_c\phi. \tag{A13}$$

In Appendix C, we explicitly show how Eq. (A5) reduces in the special case of $\hat{g}^{ab} = \tilde{g}^{ab} = g^{ab}$ to the Einstein equations in the generalized harmonic formulation with constraint damping.

2. Term: α

We next consider the terms that involve α. There are no second derivative terms on the metric, so we have

$$A_{ab}{}^{cd} = 0 \tag{A14}$$

$$B_{ab} = 0, \tag{A15}$$

$$C^{cd} = 0. \tag{A16}$$

The nonzero terms are

$$D = 2\alpha(\phi)(Xg^{00} - \nabla^0\phi\nabla^0\phi), \tag{A17}$$

$$F_{ab}^{(g)} = -2\alpha(\phi)X\nabla_a\phi\nabla_b\phi - \alpha(\phi)X^2 g_{ab} \tag{A18}$$

$$F^{(\phi)} = 4\alpha(\phi)(Xg^{\alpha 0} - \nabla^\alpha\phi\nabla^0\phi)\partial_\alpha\partial_0\phi + 2\alpha(\phi)(Xg^{\alpha\beta} - \nabla^\alpha\phi\nabla^\beta\phi)\partial_\alpha\partial_\beta\phi$$
$$- 2\alpha(\phi)(Xg^{cd} - \nabla^c\phi\nabla^d\phi)\Gamma_{ab}^c\partial_c\phi - 3\alpha'(\phi)X^2. \tag{A19}$$

3. Term: β

Finally we consider the terms that involve the Gauss-Bonnet scalar. Due to the length of the necessary algebraic manipulations, we write things out in stages. First we expand

$$R^{ij}{}_{ef} = g^{jk}R^i{}_{kef},$$
$$= g^{jk}(\partial_e\Gamma_{kf}^i - \partial_f\Gamma_{ke}^i + \Gamma_{el}^i\Gamma_{kf}^l - \Gamma_{fl}^i\Gamma_{ke}^l)$$
$$= \frac{1}{2}g^{jk}g^{im}(\partial_e\partial_k g_{mf} + \partial_e\partial_f g_{mk} - \partial_e\partial_m g_{kf} - \partial_f\partial_k g_{me} - \partial_f\partial_e g_{mk} + \partial_f\partial_m g_{ke})$$
$$+ g^{jk}(\partial_e g^{im}\Gamma_{mkf} - \partial_f g^{im}\Gamma_{mke} + \Gamma_{el}^i\Gamma_{kf}^l - \Gamma_{fl}^i\Gamma_{ke}^l) \tag{A20a}$$

$$\nabla^g\nabla_c\beta(\phi) = g^{gl}(\partial_l\partial_c\beta(\phi) - \Gamma_{lc}^m\partial_m\beta(\phi)) = g^{gl}(\beta'(\phi)[\partial_l\partial_c\phi - \Gamma_{lc}^m\partial_m\phi] + \beta''(\phi)\partial_l\phi\partial_c\phi). \tag{A20b}$$

We find that

$$2\delta_{ijg(a}^{efcd}g_{b)d}R^{ij}{}_{ef}\nabla^g\nabla_c\beta(\phi) - \delta_{ijg}^{efc}R^{ij}{}_{ef}\nabla^g\nabla_c\beta(\phi)g_{ab} = g^{jk}g^{gl}\Delta_{ijgab}^{efc}(g^{im}\partial_e\partial_k g_{mf} + \partial_e g^{im}\Gamma_{mkf} + \Gamma_{em}^i\Gamma_{kf}^m)$$
$$\times (\beta'(\phi)[\partial_l\partial_c\phi - \Gamma_{lc}^m\partial_m\phi] + \beta''(\phi)\partial_l\phi\partial_c\phi), \tag{A21}$$

where we have defined the tensor,

$$\Delta^{efc}_{ijgab} \equiv 2(2\delta^{efcd}_{ijg(a}g_{b)d} - \delta^{efc}_{ijg}\,g_{ab}), \tag{A22}$$

which is antisymmetric on the top three and first bottom three indices, and symmetric for the rightmost two bottom indices.

It turns out that while the EOMs for 4∂ST gravity are fully nonlinear, they are linear with respect to repeated derivatives; e.g. there are no terms like $(\partial_0^2 g_{ab})(\partial_0^2 \phi)$ or $(\partial_0^2 g_{ab})^2$ in the equations of motion (see Appendix B for an explicit calculation; we note that this property holds more generally for all Horndeski gravity theories [51,52]). Thus, there is no ambiguity in computing terms like $A_{ab}{}^{cd}$ and B_{ab}.

From Eq. (A21) we have

$$A_{ab}{}^{cd} = g^{j0}\Delta^{0d\gamma}_{ijgab}g^{lg}g^{ic}(\beta'(\phi)[\partial_l\partial_\gamma\phi - \Gamma^m_{l\gamma}\partial_m\phi] + \beta''(\phi)\partial_l\phi\partial_\gamma\phi), \tag{A23}$$

$$B_{ab} = g^{g0}g^{jk}\Delta^{\gamma\rho0}_{ijgab}(g^{im}\partial_\gamma\partial_k g_{m\rho} + \partial_\gamma g^{im}\Gamma^m_{mk\rho} + \Gamma^i_{\gamma m}\Gamma^m_{k\rho})\beta'(\phi) \tag{A24}$$

$$F_{ab} = g^{jk}g^{gl}\Delta^{efc}_{ijgab}(g^{im}\partial_e\partial_k g_{mf} + \partial_e g^{im}\Gamma^m_{mkf} + \Gamma^i_{em}\Gamma^m_{kf})(\beta'(\phi)[\partial_l\partial_c\phi - \Gamma^m_{lc}\partial_m\phi] + \beta''(\phi)\partial_l\phi\partial_c\phi)$$
$$- A_{ab}{}^{cd}\partial_0^2 g_{cd} - B_{ab}\partial_0^2\phi. \tag{A25}$$

We next look at the scalar field EOM. The Gauss-Bonnet scalar is

$$\mathcal{G} \equiv \frac{1}{4}\delta^{pqrs}_{ghij}R^{gh}{}_{pq}R^{ij}{}_{rs}$$
$$= \delta^{pqrs}_{ghij}(g^{hk}g^{gm}\partial_p\partial_k g_{mq} + g^{hk}\partial_p g^{gm}\Gamma^m_{mkq} + g^{hk}\Gamma^g_{pm}\Gamma^m_{kq})(g^{jv}g^{iw}\partial_r\partial_v g_{ws} + g^{jv}\partial_r g^{iw}\Gamma^m_{wvs} + g^{jv}\Gamma^i_{rw}\Gamma^w_{vs}). \tag{A26}$$

We then have

$$D = 0, \tag{A27}$$

and

$$C^{cd} = 2\beta'(\phi)\delta^{\alpha\beta0d}_{ghij}(g^{hk}g^{gm}\partial_\alpha\partial_k g_{m\beta} + g^{hk}\partial_\alpha g^{gm}\Gamma^m_{mk\beta}$$
$$+ g^{hk}\Gamma^g_{\alpha m}\Gamma^m_{k\beta})g^{j0}g^{ic}, \tag{A28}$$

$$F^{(\phi)} = \beta'(\phi)\mathcal{G} - C^{cd}\partial_0^2 g_{cd}. \tag{A29}$$

APPENDIX B: PROPERTIES OF THE PRINCIPAL PART OF ESGB GRAVITY

The evolution equations for ESGB gravity, Eqs. (7) and (8), form a fully nonlinear system of partial differential equations. It turns out though (and this is a general property of the EOMs of Horndeski gravity theories) that the EOMs do not contain terms with repeated derivatives, e.g. terms like $(\partial_c\partial_c g_{ab})^2$. In this section, we review the derivation of this fact. We consider the equations in the form of Eq. (11).

(i) $A_{ab}{}^{cdef}$: The only second order derivative term is from $\partial_l\partial_p\phi$. Consider then $c = d = l = p = Z$. We then have $\delta^{ZqZf}_{ghij} = 0$ and $\delta^{ZZf}_{gij} = 0$.

(ii) $B_{ab}{}^{cd}$: The only nonzero second order term is $\partial_e\partial_k g_{mf}$. Set then $c = d = e = k = Z$. We then have $\delta^{ZZef}_{ghij} = 0$ and $\delta^{ZZf}_{gij} = 0$.

(iii) C^{cdef}: The only term second order in derivatives is $\partial_p\partial_k g_{mq}$. Set $c = d = p = k = Z$. We then have $\delta^{ZqZf}_{ghij} = 0$.

(v) $D^{ab} = 0$ for all a, b.

APPENDIX C: REDUCTION OF MODIFIED HARMONIC FORMULATION TO GENERALIZED HARMONIC FORMULATION

For reference, here we demonstrate how the EOMs for GR in the MGH formulation reduce to those of a generalized harmonic formulation for the special choice that $\hat{g}^{ab} = \tilde{g}^{ab} = g^{ab}$. Beginning with Eqs. (A7) and (A8), we set $\tilde{g}^{ab} = \hat{g}^{ab} = g^{ab}$ to obtain

$$A_{ab}{}^{cdef} = \delta^e_a\delta^f_b g^{cd}, \tag{C1}$$

$$\hat{P}_c{}^d{}_{ab} - \frac{1}{2}g_{ab}\hat{P}_c{}^d = g_{c(a}\delta^d_{b)}, \tag{C2}$$

so that the Einstein equations given by Eq. (A5) become

$$
\begin{aligned}
-\frac{1}{2}g^{cd}\partial_c\partial_c\partial_d g_{ab} &- \frac{1}{2}\partial_{(a}g^{cd}\partial_{b)}g_{dc} - \Gamma^c_{da}\Gamma^d_{cb} + H_d\Gamma^d_{ab} \\
&\times g_{c(a}\delta^d_{b)}(\partial_d H^c + \Gamma_{gef}g^{ef}\partial_d g^{cg} + \Gamma^c_{ef}\partial_d g^{ef} \\
&+ \Gamma^c_{dg}(H^g + g^{ef}\Gamma^g_{ef})) \\
&- \frac{1}{2}\kappa(n_a C_b + n_b C_a - (1+\rho)n_c C^c g_{ab}) \\
&= 8\pi\left(T_{ab} - \frac{1}{2}T g_{ab}\right).
\end{aligned}
\tag{C3}
$$

Simplifying, we obtain the Einstein equations in a generalized harmonic formulation with constraint damping terms (e.g. Ref. [36]),

$$
\begin{aligned}
-\frac{1}{2}g^{cd}\partial_c\partial_d g_{ab} &- \partial_c g_{d(a}\partial_{b)}g^{cd} - \nabla_{(a}H_{b)} + H_c\Gamma^c_{ab} - \Gamma^c_{da}\Gamma^d_{cb} \\
&- \frac{1}{2}\kappa(n_a C_b + n_b C_a - (1+\rho)n_c C^c g_{ab}) \\
&= 8\pi\left(T_{ab} - \frac{1}{2}T g_{ab}\right).
\end{aligned}
\tag{C4}
$$

[1] R. Abbott *et al.* (LIGO Scientific and Virgo Collaborations), arXiv:2010.14529.

[2] T. Delsate, D. Hilditch, and H. Witek, Phys. Rev. D **91,** 024027 (2015).

[3] M. Okounkova, M. A. Scheel, and S. A. Teukolsky, Classical Quantum Gravity **36,** 054001 (2019).

[4] M. Okounkova, M. A. Scheel, and S. A. Teukolsky, Phys. Rev. D **99,** 044019 (2019).

[5] S. Endlich, V. Gorbenko, J. Huang, and L. Senatore, J. High Energy Phys. 09 (2017) 122.

[6] R. Cayuso and L. Lehner, Phys. Rev. D **102,** 084008 (2020).

[7] R. P. Woodard, Scholarpedia **10,** 32243 (2015).

[8] G. W. Horndeski, Int. J. Theor. Phys. **10,** 363 (1974).

[9] L. Barack *et al.*, Classical Quantum Gravity **36,** 143001 (2019).

[10] J. F. Donoghue, Phys. Rev. D **50,** 3874 (1994).

[11] C. Burgess, Living Rev. Relativity **7,** 5 (2004).

[12] S. Weinberg, Phys. Rev. D **77,** 123541 (2008).

[13] M. Okounkova, L. C. Stein, M. A. Scheel, and D. A. Hemberger, Phys. Rev. D **96,** 044020 (2017).

[14] M. Okounkova, Phys. Rev. D **102,** 084046 (2020).

[15] J. Cayuso, N. Ortiz, and L. Lehner, Phys. Rev. D **96,** 084043 (2017).

[16] A. D. Kovacs and H. S. Reall, Phys. Rev. Lett. **124,** 221101 (2020).

[17] A. D. Kovacs and H. S. Reall, Phys. Rev. D **101,** 124003 (2020).

[18] A. D. Kovács, Phys. Rev. D **100,** 024005 (2019).

[19] P. Figueras and T. França, Classical Quantum Gravity **37,** 225009 (2020).

[20] T. P. Sotiriou and S.-Y. Zhou, Phys. Rev. D **90,** 124063 (2014).

[21] S. Arai and A. Nishizawa, Phys. Rev. D **97,** 104038 (2018).

[22] J. M. Ezquiaga and M. Zumalacárregui, Phys. Rev. Lett. **119,** 251304 (2017).

[23] R. Kase and S. Tsujikawa, Int. J. Mod. Phys. D **28,** 1942005 (2019).

[24] P. Kanti, N. Mavromatos, J. Rizos, K. Tamvakis, and E. Winstanley, Phys. Rev. D **57,** 6255 (1998).

[25] T. P. Sotiriou and S.-Y. Zhou, Phys. Rev. Lett. **112,** 251102 (2014).

[26] E. Berti, K. Yagi, and N. Yunes, Gen. Relativ. Gravit. **50,** 46 (2018).

[27] J. L. Ripley and F. Pretorius, Classical Quantum Gravity **36,** 134001 (2019).

[28] J. L. Ripley and F. Pretorius, Phys. Rev. D **101,** 044015 (2020).

[29] J. F. Delgado, C. A. Herdeiro, and E. Radu, J. High Energy Phys. 04 (2020) 180.

[30] A. Sullivan, N. Yunes, and T. P. Sotiriou, arXiv:2009.10614.

[31] R. Benkel, T. P. Sotiriou, and H. Witek, Classical Quantum Gravity **34,** 064001 (2017).

[32] R. Benkel, T. P. Sotiriou, and H. Witek, Phys. Rev. D **94,** 121503 (2016).

[33] H. Witek, L. Gualtieri, P. Pani, and T. P. Sotiriou, Phys. Rev. D **99,** 064035 (2019).

[34] M. Okounkova, Phys. Rev. D **100,** 124054 (2019).

[35] C. Gundlach, J. M. Martin-Garcia, G. Calabrese, and I. Hinder, Classical Quantum Gravity **22,** 3767 (2005).

[36] F. Pretorius, Classical Quantum Gravity **22,** 425 (2005).

[37] L. Lindblom and B. Szilagyi, Phys. Rev. D **80,** 084019 (2009).

[38] M. W. Choptuik and F. Pretorius, Phys. Rev. Lett. **104,** 111101 (2010).

[39] W. E. East, F. Pretorius, and B. C. Stephens, Phys. Rev. D **85,** 124010 (2012).

[40] H. O. Kreiss and J. Oliger, Tellus **24,** 199 (1972).

[41] F. Pretorius, Classical Quantum Gravity **23,** S529 (2006).

[42] M. J. Berger and J. Oliger, J. Comput. Phys. **53,** 484 (1984).

[43] F. Pretorius and M. W. Choptuik, J. Comput. Phys. **218,** 246 (2006).

[44] F. Pretorius, B. Stephens, and M. W. Choptuik, PAMR, http://laplace.physics.ubc.ca/Group/Software.html.

[45] G. B. Cook and M. A. Scheel, Phys. Rev. D **56,** 4775 (1997).

[46] G. B. Cook, Living Rev. Relativity **3,** 5 (2000).

[47] R. P. Kerr, Phys. Rev. Lett. **11,** 237 (1963).

[48] W. E. East, F. M. Ramazanoglu, and F. Pretorius, Phys. Rev. D **86,** 104053 (2012).

[49] E. Poisson, *A Relativist's Toolkit: The Mathematics of Black-Hole Mechanics* (Cambridge University Press, Cambridge, England, 2004).

[50] O. Sarbach and M. Tiglio, Living Rev. Relativity **15**, 9 (2012).

[51] G. Papallo and H. S. Reall, Phys. Rev. D **96**, 044019 (2017).

[52] G. Papallo, Phys. Rev. D **96**, 124036 (2017).

[53] T. Giannakopoulos, D. Hilditch, and M. Zilhao, Phys. Rev. D **102**, 064035 (2020).

[54] J. L. Ripley and F. Pretorius, Phys. Rev. D **99**, 084014 (2019).

[55] G. Allwright and L. Lehner, Classical Quantum Gravity **36**, 084001 (2019).

[56] A. D. Kovacs and H. S. Reall (private communication).

[57] T. Kobayashi, M. Yamaguchi, and J. Yokoyama, Prog. Theor. Phys. **126**, 511 (2011).

[58] A. Ijjas and P. J. Steinhardt, Phys. Lett. B **764**, 289 (2017).

[59] P. Creminelli, A. Nicolis, and E. Trincherini, J. Cosmol. Astropart. Phys. 11 (2010) 021.

[60] T. Clifton, P. G. Ferreira, A. Padilla, and C. Skordis, Phys. Rep. **513**, 1 (2012).

[61] T. Kobayashi, Rep. Prog. Phys. **82**, 086901 (2019).

[62] S. Hawking, G. Ellis, and P. Landshoff, *The Large Scale Structure of Space-Time*, Cambridge Monographs on Mathematical Physics (Cambridge University Press, Cambridge, England, 1973).

[63] Y. Ageeva, P. Petrov, and V. Rubakov, J. High Energy Phys. 12 (2020) 107.

[64] www.scinethpc.ca/.

[65] www.computecanada.ca.